Turbulence-permitting air pollution simulation for the Stuttgart metropolitan area

Thomas Schwitalla*[1], Hans-Stefan Bauer[1], Kirsten Warrach-Sagi[1], Thomas Bönisch[2], Volker Wulfmeyer[1]

[1] Institute of Physics and Meteorology, University of Hohenheim, Garbenstrasse 30, 70599 Stuttgart, Germany.

[2] High-Performance Computing Center Stuttgart (HLRS), Nobelstrasse 19, 70569 Stuttgart, Germany

Correspondence to: Thomas Schwitalla (thomas.schwitalla@uni-hohenheim.de)

Abstract. Air pollution is one of the major challenges in urban areas. It can have a major impact on human health and society and is currently a subject of several litigations at European courts. Information on the level of air pollution is based on near surface measurements, which are often irregularly distributed along the main traffic roads and provide almost no information about the residential areas and office districts in the cities. To further enhance the process understanding and give scientific support to decision makers, we developed a prototype for an air quality forecasting system (AQFS) within the EU demonstration project "Open Forecast".

For AQFS, the Weather Research and Forecasting model together with its coupled chemistry component (WRF-Chem) is applied for the Stuttgart metropolitan area in Germany. Three model domains from 1.25 km down to a turbulence permitting resolution of 50 m were used and a single layer urban canopy model was active in all domains. As demonstration case study the 21 January 2019 was selected which was a heavy polluted day with observed PM_{10} concentrations exceeding 50 µg m^{-3}.

Our results show that the model is capable to reasonably simulate the diurnal cycle of surface fluxes and 2-m temperatures as well as evolution of the stable and shallow boundary layer typically occurring in wintertime in Stuttgart. The simulated fields of particulates with a diameter of less than 10 µm (PM_{10}) and Nitrogen dioxide (NO_2) allow a clear statement about the most heavily polluted areas apart from the irregularly distributed measurement sites. Together with information about the vertical distribution of PM_{10} and NO_2 from the model, AQFS will serve as a valuable tool for air quality forecast and has the potential of being applied to other cities around the world.

1. Introduction

Currently more than 50 % of the global population live in cities whereas the United Nations (UN) expect a further increase by about 10 % in 2030 (UN, 2018). The UN also expect that in 2030 34% of the world population will reside in cities with more than 500 000 inhabitants.

Due to a strong increase of road traffic in major European cities (Thunis et al., 2017), pollution limits are often violated in larger cities. E.g. for particulate matter with particle diameters less than 10 µm (PM_{10}), the critical value is an annual mean concentration of 20 µg m^{-3} or a daily mean value of 50 µg m^{-3} (WHO, 2005). For Nitrogen dioxide (NO_2) the critical values are 200 µg m^{-3} and 40 µg m^{-3} as daily and annual mean values, respectively.

The violation of these pollution limits canlead to health and environmental problems and is currently part of several litigations e.g. at the German Federal Administrative Court dealing with possible driving bans for non low-emission vehicles. The basis for these litigations are mostly few local, unevenly distributed observations which . In combination with special meteorological conditions like winter time thermal inversion layers it can be misleading to conclude about the overall air quality in the city only from single observations. According to e.g. the German Federal Immission Control Ordinance[1] it is sufficient that traffic related measurements are representative for a section of 100 m, but this is not representative for the commercial and office districts in the cities that are suffering from traffic control in case of fine dust alerts and residential areas. Namely in residential areas health protection action plans require representative air quality measures.

Therefore, it becomes important to apply a more scientifically valid approach by applying coupled atmospheric and chemistry models to predict air quality. Regional and global atmospheric models like the Weather Research and Forecasting (WRF) model (Skamarock et al., 2019), the Consortium for Small Scale modeling (COSMO; Baldauf et al., 2011), the Icosahedric Nonhydrostatic model (ICON; Zängl et al., 2015), or the Regional Climate Model system (RegCM4; Giorgi et al., 2012) are often used to force offline chemistry transport models like CHIMERE (Mailler et al., 2017), LOTOS-EUROS (Manders et al., 2017), EURopean Air Pollution Dispersion (EURAD; Memmesheimer et al., 2004), and Model for OZone And Related chemical Tracers (MOZART) (Brasseur et al., 1998; Horowitz et al., 2003).

Several studies showed that combining an atmospheric model with an online coupled chemistry component is a suitable tool for air quality and pollution modeling in urban areas at the convection permitting (CP) resolution (Fallmann et al., 2014; Kuik et al., 2016; Zhong et al., 2016; Kuik et al., 2018; Huszar et al., 2020) .

Compared to chemical transport models, coupled models like WRF-Chem (Grell et al., 2005), COSMO-ART (Vogel et al., 2009), ICON-ART (Rieger et al., 2015), and the Integrated Forecasting System (IFS) MOZART (Flemming et al., 2015) allow for a direct interaction of aerosols with radiation leading to a better representation of the energy balance closure at the surface as it would be the case when applying an offline chemistry model.

As usually the terrain and land cover over urban areas show fine scale structures which are not resolved even by a CP resolution, there is a need for turbulence permitting (TP) simulations with horizontal grid increments of a few hundred meters or even less. Important features are, e.g., urban heat island effects (Fallmann et al., 2014; Fallmann et al., 2016; García-Díez et al., 2016; Li et al., 2019) and local wind systems like mountain and valley winds due to differential heating (Corsmeier et al., 2011; e.g. Jin et al., 2016). Also, micro- and mesoscale wind systems can develop due to urban structures and the heterogeneity of the land surface. It is well known that TP simulations are a promising tool to further enhance the understanding of processes in the atmospheric boundary layer (Heinze et al., 2017b; Panosetti et al., 2016; Heinze et al., 2017a; Bauer et al., 2020) in urban areas (Nakayama et al., 2012; Maronga et al., 2019; Maronga et al., 2020).

In order to further enhance the quality of the simulations, building and urban canopy models (UCM) are developed (Martilli et al., 2002; Kusaka and Kimura, 2004; Salamanca and Martilli, 2010; Maronga et al., 2019; Scherer et al., 2019; Teixeira et al., 2019). The main purpose of UCMs is to provide a better description of the lower

[1] https://www.gesetze-im-internet.de/bimschv_39/anlage_3.html

boundaries over urban areas such as building, roof and road geometries and their interactions with atmospheric water vapor, wind, and radiation.

With the EU-funded project Open Forecast (https://open-forecast.eu/en/) it was intended to develop a prototype for an air quality forecasting system (AQFS) for the Stuttgart metropolitan area in southwest Germany. Open Forecast is a demonstration project to show the potential of open data combined with supercomputer resources to create new data products for European citizens and public authorities. The long-term goal is to provide end users and political decision-makers a useful tool, particularly considering further urbanization, heat island effects as well as potential driving restrictions due to recent EU decisions on emission limits.

For our AQFS we use the WRF-Chem NWP model (Grell et al., 2005; Skamarock et al., 2019) as the WRF model is extensively evaluated over Europe at different time scales and horizontal resolutions (San José et al., 2013; Warrach-Sagi et al., 2013; Milovac et al., 2016; Lian et al., 2018; Molnár et al., 2019; Bauer et al., 2020; Coppola et al., 2020; Schwitalla et al., 2020). It can easily be set up in a nested configuration over all regions of the Earth. Compared to PALM-4U model, the nested model domains are driven by the full atmospheric and chemical information from the parent domain along its lateral boundaries. Also, it contains well-characterized combinations of parameterizations of turbulence and cloud microphysics in the outer domain that are consistent with the inner TP domains where the high-quality cloud parameterization remains. No switch between different model systems is required, which is expected to provide a great advantage with respect to the skill of air pollution and meteorological forecasts.

To enhance the forecast skill, suitable variational and ensemble-based data assimilation systems are already in place to further improve the meteorological initial conditions (Barker et al., 2012; Zhang et al., 2014; Kawabata et al., 2018; Thundathil et al., 2020) and the chemical initial conditions (Chen et al., 2019; Sun et al., 2020) but this is beyond the scope of our study.

The Parallelized Large-Eddy Simulation Model (PALM) model (Maronga et al., 2015) is another widely used TP simulation model over Europe. PALM did not include the full interaction between land-surface, radiation, cloud microphysics and chemistry during the performance of our study. The very recent version 6.0 of PALM-4U (PALM for urban applications) (Maronga et al., 2020) is expected to contain a fully coupled chemistry module (Khan et al., 2020).

Fallmann et al. (2016) and Kuik et al. (2016) performed air quality simulations with WRF-Chem over the cities of Berlin and Stuttgart on a CP resolution down to 1km and less than 40 model levels. They used the TNO-MACC emission inventory (Kuenen et al., 2014) which is available as an annual totals on a 7 km x 7 km resolution. As the topography of Stuttgart is very complex, the AQFS applies the WRF-Chem model on a turbulence permitting horizontal resolution using 100 model levels to account for the shallow boundary layer occurring during wintertime. In addition, we applied a local emission data set from the Baden-Württemberg State Institute for the Environment, Survey and Nature Conservation available as annual mean on a horizontal resolution of 500 m x 500 m to resolve fine-scale emission structures.

Our study focuses on the methodology how to set up a AQFS prototype by using WRF-Chem and its application to a typical wintertime situation in the Stuttgart metropolitan area. The manuscript is set up as follows: section 2 describes the design of our AQFS model system on the turbulence permitting resolution of 50 m followed by a

description of the selected case study. Section 4 shows the results including a discussion, sect. 5 summarizes our work and provides an outlook on potential future enhancements of the AQFS prototype.

2. AQFS design

2.1. WRF model set-up

For our AQFS, we selected the Advanced Research WRF-Chem model in version 4.0.3 (Grell et al., 2005; Skamarock et al., 2019). To reach the targeted resolution of 50 m, three model domains have been applied with horizontal resolutions of 1250 m, 250 m, and 50 m and encompasses 800*800 grid cells in the outer domain and 601*601 grid cells in the two inner TP domains. The reasons to start with a resolution of 1250 m in the outermost domain is 1) to avoid the application of a convection parametrization which can deteriorate the model results (Prein et al., 2015; Coppola et al., 2020), 2) that the model starts to partially resolve turbulent structures whilst a PBL parametrization is still necessary (Honnert and Masson, 2014; Honnert et al., 2020), and 3) to reach the target resolution with a nesting ratio of 5:1. The areas of model domain 1 and 3 are shown in Fig. 1.

As seen from Fig. 1b, the Stuttgart metropolitan area is characterized by an elevation variation of more than 300 m. The lowest elevation is approx. 220 m in the basin while the highest elevation reaches up to 570 m. As the main traffic roads are in the basin, especially during wintertime this often leads to a worsening of the air quality as the surrounding prevents an air mass exchange due to the stationary temperature inversion.

For the WRF model system land cover and soil texture fields are not available at resolutions higher than 500m. Therefore we reclassified land cover data from the Copernicus CLC 2012 data set (European Union, 2012), available on a resolution of 100 m, from the original 44 categories to the categories applied in the WRF model for the simulations of the outer 2 domains. For the innermost model domain, we incorporated the most recent high-resolution land-cover data set from the Baden-Württemberg State Institute for the Environment (LUBW), which is derived from Landsat (Butcher et al., 2019) in 2010 and is available at 30 m resolution (https://udo.lubw.baden-wuerttemberg.de/public/) This data set was also reclassified to the corresponding land cover categories used in WRF and is shown in Fig. 2.

The resolution of the provided default Food and Agriculture Organization of the United Nations (FAO) soil texture data is only 10 km, therefore we used soil texture data from the International Soil Reference and Information Centre (ISRIC) SoilGrids project (Hengl et al., 2014; Hengl et al., 2015). These data are available on a resolution of 250 m. Terrain information was provided by the National Center for Atmospheric Research (NCAR) derived from the Global multi-resolution terrain elevation data 2010 (GMTED2010) data set (Danielson and Gesch, 2011) for domain 1. As the horizontal resolution of the GMTED2010 data set is 1 km, the 3" gap-filled Shuttle Radar Topography Mission (SRTM) data set (Farr et al., 2007) is used for domain 2. As this resolution is still too coarse for our targeted resolution of 50 m, the Digital Elevation model Europe (EU-DEM; European Union, 2017), available at a resolution of 25 m, is used for the innermost domain.

In our set-up, we use 100 vertical levels for all domains using the traditional terrain following coordinate system in WRF; 20 of the levels are distributed in the lowest 1100 m above ground level (AGL). All domains apply the Noah-MP land surface model (Niu et al., 2011; Yang et al., 2011), the revised MM5 surface layer scheme based on Monin-Obukhov similarity theory (Jiménez et al., 2012), the Thompson 2-moment cloud microphysics scheme (Thompson et al., 2008) and the Rapid Radiative Transfer Model for GCMs (RRTMG; Iacono et al., 2008) for

parametrizing longwave and shortwave radiation. Due to the coarser resolution of the outermost domain, we applied the Yonsei University (YSU; Hong et al., 2006) planetary boundary layer (PBL) parametrization in D01 only. As suggested by the WRF user guide, we applied the sub-grid turbulent stress option for momentum (Kosovic, 1997) in domains two and three. The complete namelist settings are provided in the supplement.

The more sophisticated Building Effect Parameterization (BEP; Martilli et al., 2002) is not applied as this scheme does not work with our selection of parametrizations. Instead, the single layer urban canopy model (UCM) (Kusaka and Kimura, 2004) is selected to improve the representation of the urban canopy layer and the surface fluxes. The parameters needed by the UCM are read in from the lookup table URBPARAM.TBL which was adjusted for the Stuttgart area following Fallmann (2014).

Atmospheric chemistry is parametrized by the Regional Acid Deposition Model 2nd generation (RADM2) model (Stockwell et al., 1990). RADM2 features more than 60 chemical species and more than 135 chemical reactions including photolysis. Aerosols are represented by the Modal Aerosol Dynamics Model for Europe (MADE) and Secondary Organic Aerosol Model (SORGAM) scheme (Ackermann et al., 1998; Schell et al., 2001) considering size distributions, nucleation, coagulation, and condensational growth. The combination of RADM2_MADE-SORGAM is a computationally efficient approach and is widely used for simulations over Europe (Forkel et al., 2015; Mar et al., 2016). To further enhance vertical mixing of CO to higher altitudes during nighttime over urban grid cells, the if-statements in the dry deposition driver of WRF-Chem at lines 690 and 707 have been deleted according as shown in the supplement of Kuik et al. (2018).

Compared to a previous study from (Fallmann et al., 2016), who performed simulations over the Stuttgart metropolitan area using WRF-Chem on a CP resolution of 3 km, or the study of (Kuik et al., 2016) who performed a three month simulation at different resolutions over Berlin, simulations on the TP resolution provide a much more realistic representation of the land-cover structures (see Fig. 2 in this paper and e.g. Fig. 2b in Fallmann et al. (2016)). As the climate in the Stuttgart metropolitan area is strongly influenced by the topography, we are convinced that our special combination of a TP resolution and high-resolution emission data (see section 2.3) will lead to a better understanding and prediction of the air pollution situation in this area.

Currently, air pollution modeling with WRF-Chem is a computationally expensive task. Depending on the number of output variables and frequency (5 min in our study), a 24 h simulation currently takes around 36 h wall clock time. For future experiments it is worth to try the I/O quilting option in combination with PNetCDF which should considerably reduce the time spent on I/O.

While the WRF model itself is ready for hybrid parallelism (MPI + OpenMP), the WRF-Chem model can only be used with MPI. If WRF-Chem could be enhanced for additional OpenMP capabilities, this would lead to an increase in computation speed almost linear with the number of OpenMP threads.

Due to the complexity of the chemistry model in combination with the very high horizontal resolution and the calm meteorological conditions, the adaptive model time step option was chosen instead of a fixed time step. Model output is available in 5 min intervals for the innermost model domain.

Our single day case study on the turbulence permitting (TP) scale is designed to serve as a test bed to set up an air quality forecasting system prototype for the Stuttgart metropolitan area. For process studies, the model chain itself can be applied to other areas over the globe as long as 1) detailed land cover and soil texture data are available, 2)

high-resolution emission data not only from traffic are available. The new model system can be even applied in a forecast and warning mode, if near real time emission data exist. As the computational demands of applying WRF-Chem on the TP scale are very high, access to an HPC system is a prerequisite.

2.2. Model initialization

The meteorological initial and boundary conditions were provided by the operational ECMWF integrated forecasting system (IFS) analysis on model levels. The IFS is a global model with 9 km horizontal resolution and applies a sophisticated four-dimensional variational (4DVAR) data assimilation system (Bonavita et al., 2016). The data have been retrieved from the ECMWF Meteorological Archival and Retrieval System (MARS) and were interpolated to a resolution of 0.05°.

The initialization and provision of the boundary conditions of the chemistry of the model is done with data from the Whole Atmosphere Community Climate Model (WACCM; Marsh et al., 2013) using the Model for Ozone and Related Chemical Tracers (MOZART) conversion tool MOZBC (Pfister et al., 2011). As the resolution of WACCM is very coarse, the input data was enhanced by the ECMWF Copernicus Atmosphere Monitoring Service (CAMS) reanalysis data set on 60 model levels and 40 km horizontal resolution (Inness et al., 2019).

2.3. Emission data

The emission data set used in this study is a combination of three products. Global input data sets containing coarse resolution emissions from different sources are obtained from the BRAMS numerical modeling system (Freitas et al., 2017).The PREP-CHEM-SRC tool (Freitas et al., 2011) is then applied as pre-processor to convert these emissions to the appropriate WRF units and interpolate the data onto the WRF model grid.

As global emission data sets have a very coarse resolution in space and time, higher resolution emission data for Europe from the Copernicus Atmosphere Monitoring Service (CAMS; Copernicus) CAMS-REG-AP product became available (Granier et al., 2019). Its resolution is approx. 7x7 km and it is based on total annual emissions from 2016. This product provides emissions of PM_{10}, $PM_{2.5}$, SO_2, CO, NO_x, and CH_4 and contains sources from different sectors, separated into ten different categories following the Gridded Nomenclature For Reporting (GNFR; Granier et al., 2019).

The third emission data set (BW-EMISS) deployed in our study was obtained from the Baden-Württemberg State Institute for the Environment (LUBW). This data set contains annual mean emissions from different sectors following the GNFR classification and is currently available only until 2014 and has a horizontal resolution of 500 m. Unfortunately, more recent quality-controlled data sets were not available when our study was performed. It is expected that annual emissions for 2018 will become available by mid of 2021.

As CAMS-REG-AP and BW-EMISS only contain annual sums or annual mean values, a temporal decomposition was applied for both data sets following Denier van der Gon et al. (2011). Depending on the GNFR code, the data are first projected onto the corresponding month, followed by the corresponding day of the week and the hour of the day. A similar approach was performed e.g. in Resler et al. (2020, under review) for the city of Prague. After finishing the decomposition, the data are converted to the corresponding units and interpolated onto the WRF model grid using the Earth System Modeling Framework (ESMF; Valcke et al., 2012) interpolation utilities.

Figure 3 shows an example of the NO_2 emissions derived from the CAMS-REG-AP product (left) and the emission data derived from the LUBW data set (right) on January 21, 2019 at 07 UTC.

Due to its much higher horizontal resolution, the BW-EMISS data set (Fig. 3b) shows much more detailed structures for the NO_2 emissions which are mainly caused by road traffic. The average emissions for this particular time step are 2 mol km^{-2} h^{-1} for the CAMS-REG-AP data set and 7 mol km^{-2} h^{-1} for the BW-EMISS data set.

In addition, the following adjustments have been performed: 1) NO_x emissions from forest grid cells have been reduced by 90 %, 2) Road traffic NO_x emissions were transformed into 90 % NO and 10 % NO_2 emissions following Kuik et al. (2018) 3) All emissions from Stuttgart airport were reduced by 90 % during the nighttime flight ban between 00 UTC and 04 UTC as well as after 21 UTC.

The WRF-Chem model only ingests one emission data set per species, hence emissions from the different GNFR categories have been accumulated to a single emission data set before performing the simulation. Figure 4 summarizes all necessary steps and the complete data and workflow of the AQFS prototype.

2.4. Observations

We used data from three meteorological stations (Stuttgart-Schnarrenberg (48.8281°N 9.2°E, elevation 314 m), Stuttgart Airport (48.6883°N 9.2235°E, elevation 375 m), and Institute of Physics and Meteorology (IPM) at the University of Hohenheim (48.716°N 9.213°E, elevation 407 m) to validate the simulated 2m temperatures; data are available every 10 minutes. The locations are indicated by the black dots in Fig. 1b. In addition, the radiosonde data from Stuttgart-Schnarrenberg were used.

3. Case study description

For our study, we selected 21 January 2019. This day was characterized as “fine dust alarm” situation (Stuttgart Municipality and German Meteorological Service (DWD), 2019) which is defined by a combination of the following criteria:

1. Expected daily maximum PM_{10} concentration at Stuttgart Neckartor (NT in Fig. 1b) is higher than 30 µg m^{-3}
2. No rain on the following day
3. 10-m wind speed less than 3 m s^{-1} from south to northwest directions (180-330 °)
4. Nocturnal atmospheric inversion
5. Mixing layer depth less than 500 m during the day
6. Daily average 10-m wind speed less than 3 m s^{-1} from all directions

A sufficient criterion is a higher PM_{10} concentration following (1). If (1) is not fulfilled, then (2) and (3) together with either (4) and/or (5) has to be fulfilled. If only (4) or (5) is fulfilled, then (6) has to be considered. For our case study, the criteria 1-5 were fulfilled.

The thick lines in Fig. 5 shows the observed PM_{10} and NO_2 concentrations at several stations in our model domain. From Fig. 5a the high NO_2 concentrations at Neckartor and Hohenheimer Strasse occurring after sunrise can be clearly identified. While these measurements are taken next to main roads, the other stations show considerably lower NO_2 concentrations throughout the day. The PM_{10} concentrations (Fig. 5b) show extremely high values at

Neckartor exceeding 100 µg m^{-3} around noon time and the evening rush hour which clearly meets the main criteria of the "fine dust alarm situation". The other stations, which are not directly taken near main roads with heavy traffic show considerably lower PM_{10} concentrations around 40 µg m^{-3} .

This day was a typical winter weather situation. Central Europe was located at the east flank of a blocking high pressure system located over the East Atlantic together with moderate to low horizontal geopotential gradients and resulting weak winds at 500 hPa in southwestern Germany (Fig. 6a).

Near surface temperatures are below freezing level, between 1000 and 850 hPa very light easterly winds characterize the flow, and a dry layer is present around 925 hPa (Fig. 6b). Above 850 hPa, the wind direction rapidly changes to westerly directions, but the wind speeds remain below 5 m s^{-1} (see Fig. 7a).

The inversion between the two air masses inhibits vertical mixing leading to higher concentrations of aerosols in the lowest few hundred meters above ground (AGL) and preventing air mass exchange aloft. This inversion is further enhanced by the special orography of Stuttgart city (see later Fig. 15).

4. Results and Discussion

4.1. Meteorological quantities

Figure 7a shows a Skew-T diagram of the model initial conditions (black line) at Stuttgart-Schnarrenberg valid at 00 UTC 21 January 2019 in comparison with the observations (red line).

The initial conditions agree well with the sounding showing a weak temperature inversion around 900 hPa with high relative humidity values up to 650 hPa. The observed and simulated lifting condensation level is 940 hPa and the integrated water vapor (PWAT) is 8 mm. Wind speed and direction agree with the observations showing a wind shear above 850 hPa associated with low wind speeds of less than 5 m s^{-1}.

To further evaluate the stratification conditions during the day, Figure 7b shows the observed and simulated temperature, dew point, and wind profiles at 11 UTC. The vertical structure of the observation and the simulation has an almost perfect agreement. The temperature inversion layer at 910 hPa is well captured although the simulated temperatures below the inversion are too high by about 1.5 K. The humidity profile (expressed as dewpoint profile) is also very well captured with the largest moisture content below 870 hPa. Wind speed and direction above 850 hPa agree well with the observation throughout the atmosphere. In regard of the vertical model resolution, the wind situation in the lowest 1000 m AGL is also reasonably represented.

Figure 8 exemplarily shows the simulated 2-m temperature together with 10-m wind velocities at 12 UTC (noon time) to display the complexity of the Stuttgart metropolitan area.

The 2-m temperatures show a daytime warming of downtown Stuttgart and the Neckar Valley while still temperature slightly below 0°C are present at higher elevations (blue colors in Fig. 8). The wind situation is very complex due to weak wind speeds in combination with a shallow boundary layer (see later Fig. 16) but the wind flow along the upper Neckar river (south of 48.75°) is strongly pronounced. After sunset, wind speed starts to decrease and the channeling effect along the Neckar weakens (not shown).

Figure 9 shows an evaluation of the diurnal cycle of 2-m temperatures at the three measurement sites Schnarrenberg, IPM and airport. Sunrise is at 07 UTC and sunset at 16 UTC and the model data are averaged over

5 grid cells around the measurement site to take into account that even a simulation with 50 m resolution cannot fully capture the local conditions at the measurement site. The northern station Schnarrenberg shows a lower temperature throughout the day than the other two stations, which are situated 3 km apart at a similar elevation. The temperature is about 1 K colder during the day and 0.5 K colder during the night.

At Schnarrenberg, the observed diurnal cycle is reasonably well simulated with WRF. Between 00 and 15 UTC, a warm temperature bias of 1 K is present in the simulation, which turns into a small negative bias after sunset. At IPM, the simulation shows a cold bias until 04 UTC turning into a warm bias as the strong temperature drop is not simulated until 06:30 UTC. After 09 UTC until sunset the simulated temperature agrees well with the observations while later a cold bias of around 1 K is present.

For the airport station, the model stays too warm with a positive bias of almost 2 K between 05 and 09 UTC. During the further course of the day, the bias reduces to 1 K at noon while after sunset it turns into a negative bias of 1 K.

A possible reason for the larger differences at the airport and IPM before (after) sun rise (sun set) is the observed occurrence of low stratus or fog. At the beginning of the simulation, cloud coverage was reported by 5—7 octas (broken clouds) over Schnarrenberg and the airport at approx. 500 m AGL (not shown) while after 04 UTC the low level clouds started to diminish at Schnarrenberg first leading to a strong cooling until the early morning which is seen as a temperature decrease in the observations shown in Fig. 9. The temperature drop at Schnarrenberg and IPM is also simulated but with a delay of approx. 2 h. A reason for this delayed temperature drop could be a simulated thin cloud layer around 1000 m AGL which is present in the lower left and partly the lower right quadrant of the model domain. This cloud layer slowly moves in a southeasterly direction and starts to dissolve around 06 UTC.

During the evening transition and the following night, the low stratus is developing again at the measurement sites with a ceiling of 500 m AGL but is not simulated and thus contributes to a stronger cooling in the model. Another contributing factor to the delayed cloud dissipation could be the turbulence spin-up time (Kealy et al., 2019), but this is beyond the scope of this study.

Although no measurements of sensible heat and ground heat fluxes are available, diurnal cycles of the fluxes at the locations IPM, Schnarrenberg, airport, and Schlossplatz were investigated. Figure 10 shows the simulated surface sensible heat and ground heat flux at the four sites.

The sensible heat flux (Fig. 10a) shows a typical diurnal cycle with fluxes around zero before (after) sunrise (sunset). During the day, the model simulates typical wintertime sensible heat fluxes between 40 and 100 W/m² (e.g. Zieliński et al., 2018), which nicely shows a dependency on the different underlying land cover types. Lower sensible heat fluxes occur over the sparsely vegetated surface at the airport as compared to the cropland station IPM while the urban locations Schnarrenberg and Schlossplatz shows interjacent values. As the algorithm to diagnose the 2-m temperature in NOAHMP is rather complex, no clear correlation between SH and the 2-m temperature shown in Fig. 9 can be made. The latent heat fluxes (not shown) are almost zero at Schnarrenberg and less than 10 W m^{-2} at the other two locations due to cold and dry winter conditions

The simulated ground heat flux (Fig. 10b) shows an interesting behavior. Until sunrise, the simulated GRDFLX at the airport and IPM shows fluctuations around -50 W m^{-2} indicating some low levels clouds in accordance with

the too high simulated 2-m temperatures shown in Fig. 9. During the further course of the day, IPM and airport show a clear diurnal cycle with maximum values between 100 and 170 W m^{-2} reflected in the highest surface temperatures during the day (not shown).

At Schnarrenberg, most of the time the ground heat flux is less than zero indicating a cooling of the soil, while between 12 UTC and 16 UTC small positive values are simulated. As Schnarrenberg is categorized as low density residential (category 31) with an urban fraction of 0.5 and the UCM is applied here, energy is mainly stored in the urban canopy layer instead of being transferred into the soil. At Schlossplatz (high-density residential) the ground heat flux shows a similar shape but with a larger amplitude as compared to Schnarrenberg.

As this day was characterized by a shallow PBL and a temperature inversion, it is worth to investigate the PBL evolution during the day. Figures 11a, bshow time-height cross sections of potential temperature at IPM (top) and Schnarrenberg (bottom).

Both locations are characterized by a very stable shallow boundary layer until 09 UTC with a depth of less than 200 m. Between 03 and 09 UTC the temperatures at Schnarrenberg are up to 1.5 K colder near the surface (Fig. 9) resulting in a stronger potential temperature gradient up to 400 m AGL compared to the IPM location. During the day, the boundary layer height increases to 400 m above ground as indicated by the constant potential temperature (e.g. Bauer et al., 2020) which is a typical value for European winter conditions (Seidel et al., 2012; Wang et al., 2020). The PBL heights are also visible by the potential temperature gradients ($\Delta\theta$) shown in Figs. 11c, d. During the morning hours, a very shallow boundary layer was simulated at Schnarrenberg (blue colors in Fig. 11c) while at IPM some fluctuations are present. During daytime, $\Delta\theta$ nicely shows the PBL height evolution up to 400 m AGL, while after sunset the PBL collapses to a very stable layer again (dark blue colors in Figs. 11c, d) with heights between 50—100 m AGL. Calculating the gradient Richardson number (Ri; Chan, 2008) (not shown) and assuming a threshold of 0.25 for a turbulent PBL (Seidel et al., 2012; Lee and Wekker, 2016) leads to similar results After sunset around 15:30 UTC the boundary layer collapses to a night-time stable boundary layer and a temperature inversion occurred again.

4.2. Air quality

The most relevant air pollutants for air quality considerations in cities are NO_2 and PM_{10}. Sources for these are mainly truck supply, transit, and commuter traffic through the city as well as advection from motorways south, west, and northwest of Stuttgart.

As the incorporated emissions are from 2014 and are based on annual values, it cannot be expected that the model exactly matches the observed concentrations. For instance, the actual traffic, the sequence of traffic lights and traffic congestions of this particular day cannot be realistically represented. In addition, all diagnosed or prognostic chemical quantities are only available on model levels (with the lowest model half level being at ~15 m above ground) but according to studies of Glaser et al. (2003) and Samad et al. (2020) the concentrations of PM_{10} and NO_2 are often constant up to 150—200 m AGL during daytime.

We start with the discussion of the simulated horizontal distributions followed by vertical cross sections of NO_2 and PM_{10}.

4.2.1 Horizontal distribution

Figure 12 shows the horizontal distribution of the NO_2 concentration at the lowest model half level (~15 m AGL) at the four timesteps 07:30 UTC, 12 UTC, 18 UTC and 23 UTC 21 January 2019.

At 7:30 UTC the morning traffic rush hour is visible in the NO_2 concentrations in Fig. 12a. High NO_2 concentrations of more than 80 µg m^{-3} are simulated along the motorway A81 in the northwest of the domain, over the airport and over downtown Stuttgart. In the Neckar Valley the concentrations exceed 120 µg m^{-3}. At noon time (Fig. 12b), when turbulence is fully evolved (Fig. 11), the simulated NO_2 concentrations are less than 30 µg m^{-3} on average apparently due to vertical mixing of NO_2 (see next section). In the evening (Fig. 12c) the simulated NO_2 concentrations increase again showing values of more than 100 µg m^{-3} over the airport and more than 150 µg m^{-3} in downtown Stuttgart and the Neckar Valley due to road and air traffic. The high morning concentrations along the northwestern motorway are not reached since the wind speed increases and the near surface winds turn towards a westerly direction. According to the emission data set converted by the temporal factors, the evening traffic spreads over a longer time. During the night (Fig. 12d), NO_2 accumulates in the Stuttgart basin as well as the Neckar Valley due to the very low nocturnal boundary layer height of less than 200 m capped by an atmospheric inversion (Fig. 11).

Compared to the observed NO_2 concentrations (Fig. 5a) , the simulated concentrations during the peak traffic times are too high at Arnulf-Klett Platz, Neckartor and Hohenheimer Strasse. Possible reasons are that either the traffic is reduced and/or that the vehicle emission classification have been improved since 2014. Another contributing factor could be that the vertical mixing near the surface is too weak during sunrise and sunset while it appears slightly too strong during daytime as indicated by the very low simulated NO_2 concentrations.

Apart from NO_2, the concentration of PM_{10} is an important parameter for air quality considerations and is the decisive factor for proclaiming a “fine dust alarm” situation in Stuttgart (Stuttgart Municipality and German Meteorological Service (DWD), 2019).

Figure 13 shows the horizontal distribution of PM_{10} for the same time steps as shown in Fig 12.

During the morning traffic (Fig. 13a), PM_{10} accumulates in the Stuttgart basin as this is an area with heavy traffic during the morning and an atmospheric inversion is present (Fig. 7). Interestingly, the high NO_2 concentrations along the motorway (Fig. 12a) do not lead to very high PM_{10} concentrations potentially due to chemical transitions caused by low temperatures.

During daytime when turbulence is fully evolved, the concentration of PM_{10} decreases to less than 20 µg m^{-3} due to vertical mixing and horizontal transport (see next section). After sunset (Fig. 13c) PM_{10} starts to accumulate again in the Stuttgart basin showing concentrations between 35—40 µg m^{-3}. During the night (Fig. 13d) PM_{10} accumulates over a large part of the model domain as the nocturnal boundary layer is very shallow, an inversion layer is present 200 m AGL and the wind direction changes from north to west. In the configuration we use in our study, PM_{10} is a diagnostic variable which is a sum of the $PM_{2.5}$ concentration (which is around 26 µg m^{-3} at 23 UTC) and the other prognostic aerosol species. As the night is very cold with temperatures far below freezing and the humidity is very high, the high concentrations could imply a very (too) strong deposition or be the result of dense fog formation due to weak near-surface winds.

4.2.2 Vertical distribution of NO_2 and PM_{10}

In addition to the horizontal distribution of near surface NO_2 and PM_{10}, TP simulations with a fine vertical resolution also enable qualitative insights into the vertical distribution of pollutants. Figure 14 shows West-East

cross sections at Neckartor (Fig. 1b) during the morning rush hour and at noon time. Neckartor is one of the heaviest traffic locations in the Stuttgart city area.

The NO_2 concentration during the morning rush hour shows an accumulation along the motorway (red arrow in Fig. 14a) and in the region around Neckartor (white arrow in Fig. 14a) with concentrations exceeding 100 µg m^{-3} as the atmospheric inversion prevents exchange with the layers above (Fig. 7). The vertical extent of concentrations higher than 30 µg m^{-3} is about 200 m AGL with a strong reduction above.
During noon time (Fig. 14b), the simulated NO_2 concentration is much lower (less than 30 µg m^{-3}) as turbulence leads to a stronger mixing throughout the boundary layer up to 400 m AGL which is in accordance with the simulated potential temperature timeseries shown in Fig. 11.
Figure 15a displays the simulated PM_{10} concentrations during the morning rush hour. Similar like for NO_2, higher concentrations of more than 25 µg m^{-3} is simulated along the motorway and in the Stuttgart basin. During the day, PM_{10} is vertically mixed showing a clear gradient around 800 m above sea level (ASL) (Fig. 15b) while concentrations remain between 10-20 µg m^{-3} within the boundary layer.

Apart from the West-East cross sections it is also worthwhile to investigate the vertical temporal evolution of NO_2 and PM_{10} concentrations. Therefore, Fig. 16 shows time height cross sections of NO_2 (top) and PM_{10} (bottom) at Neckartor.

Well visible are the high simulated NO_2 and PM_{10} concentrations during the morning rush hour with peak values of more than 120 µg m^{-3} NO_2 and more than 40 µg m^{-3} PM_{10}. The high concentrations of NO_2 and PM_{10} are present up to around 150-200 m AGL. During daytime, turbulence efficiently mixes the pollutants up to higher altitude and the near surface concentrations are quickly reduced. During the evening when the very shallow boundary layer has developed again and evening traffic commences, the particle concentrations increase, and peak values of more than 30 µg m^{-3} are simulated below 100 m AGL.

5. Summary and conclusion

This paper describes the setup of an AQFS prototype using WRF-Chem for the Stuttgart Metropolitan area. Because of the complex topography in this region, this simulation system requires a very high horizontal resolution down to the turbulenc- permitting scale to represent all orographic and land cover features.

For the development of this prototype 21 January 2019 served as test case as this was a typical winter day with an atmospheric inversion. In addition, this day was characterized as "fine dust alarm" situation where the PM_{10} concentration at the station Neckartor in the Stuttgart basin was expected to exceed 30 µg m^{-3} (http://www.stadtklima-stuttgart.de/stadtklima_filestorage/download/luft/Feinstaubwerte-2019_AN.pdf). The model setup encompassed three domains down to a turbulence permitting resolution of 50 m.

The initial conditions were provided by the ECMWF operational analysis, the CAMS reanalysis and WACCM model for background chemistry. Emission data sets from CAMS-REG-AP and high-resolution data with 500 m resolution from LUBW were combined to be used in the AQFS. As current emission data sets only provide annual totals or means, a temporal decomposition following TNO was applied (Denier van der Gon et al., 2011).

For this case study, we focused on the results with respect to 2-m temperature, surface fluxes and boundary layer evolution as well as horizontal and vertical distributions of NO_2 and PM_{10}.

Our results revealed that despite the complex topography in Stuttgart, the model is in general capable to simulate a realistic diurnal cycle of 2-m temperatures although, compared to observations, differences of up to 1 K occur. Apparently the model has difficulties with the dissolution of low stratus clouds between 03 and 06 UTC which was also reported in the work of Steeneveld et al. (2015) resulting in a warm 2-m temperature bias during the morning. Although no measurements are available, the surface sensible heat fluxes show a clear diurnal cycle with the magnitude clearly depending on the underlying land cover type. The low simulated ground heat flux and its fluctuations between 00 UTC and sunrise partially confirm the fog dissolution issue but more test cases are needed for a more detailed investigation. Over grid cells where the single layer UCM is active, most of the ground heat flux is stored in the canopy layer thus not transferred into the soil. The high vertical resolution of 100 levels enables a realistic representation of the nocturnal and daytime temperature inversion with an accompanying shallow boundary layer of less than 400 m during the day.

The simulation of PM10 shows an exceedance of the 30 µg m^{-3} concentration threshold close to the Neckartor station and also fulfills the other fine dust alarm criteria shown in section 3. Compared to the usually unevenly distributed air quality measurements, the AQFS allows further insights into the spatio-temporal pollutant distribution. The horizontal distributions of NO_2 and PM_{10} at this particular day clearly indicate the main polluted areas along the motorways and in the Stuttgart basin. The special orography of Stuttgart with its basin favors the accumulation of NO_2 and PM_{10} in the morning and evening while the pollutants are well mixed to around 200-400 m AGL when the boundary layer is fully evolved.

The simulation also shows that pollutants can be advected from the motorway A81 towards Stuttgart, depending on the wind situation, potentially leading to an increase of the NO_2 and partially PM_{10} concentrations in the Stuttgart basin. As can be seen from Figs. 12 and 13, the Neckar Valley can also have a large impact on the pollutant concentration in the Stuttgart basin in case an atmospheric inversion together with prevailing easterly winds is present.

This is, to our knowledge, the first study of applying WRF-Chem on a TP resolution for an urban area. To derive more robust conclusions with respect to air pollution, more cases studies with different weather situations during winter and summer time are necessary. Nevertheless, our evaluation gives the following indications to further improve the quality of such simulations:

I. Applying high spatial and temporal resolution gridded emission data from all pollution sources in near real time to avoid extrapolating annual emissions to individual days.. This will help to enhance the simulation of the diurnal cycles of chemical species.
II. Improving the chemical background e.g. by applying higher resolution products from the CAMS European Air quality project (Marécal et al., 2015). This will help to have a more detailed structure of the chemical constituents beneficial for subsequent downscaling simulations.
III. Using a longer spin-up period and applying a larger TP model domain to further improve the spin-up of turbulence in the model
IV. Considering vertical distribution of surface emissions (e.g. Bieser et al., 2011; Guevara et al., 2020)
V. Considerably increase the number of pollutant measurements to allow more robust conclusions

The AQFS has a great potential for urban planning applications. For example, land cover could be changed from urban low density to urban high density to investigate the impact of urban re-densification e.g. on temperature and

air quality. Although no BEP can be applied on the TP resolution with our combination of parameterizations, changes of the parameters required for the single layer UCM offer the opportunity to perform sensitivity analysis with respect to different building heights, urban greening effects (Fallmann et al., 2016), or anthropogenic heating (Karlický et al., 2020). Recently, Lin et al. (2020) developed an interface to use output from high-resolution WRF simulations to force PALM 6.0 in an offline mode which could be another tool in the future to study microscale structures in urban areas.

In the future, more emphasis should also be put on an improvement of the I/O (e.g. by means of quilting) and additional OpenMP capabilities in WRF-Chem. However simulations with WRF-Chem at the TP resolution will still require around 1500-2000 compute cores for operational use due to the small numerical time step necessary.

Although air quality modeling on the TP scale is a very challenging and computationally expensive task, we are convinced that the AQFS will have a great potential to further improve process understanding and will certainly help politicians to make decisions on a more scientifically valid basis.

Code and data availability

The WRF-Chem code version 4.0.3 can be downloaded from https://github.com/wrf-model/WRF/archive/v4.0.3.tar.gz. ECMWF analysis data can be obtained from https://apps.ecmwf.int/archive-catalogue/?type=an&class=od&stream=oper&expver=1 (last access: 26 August 2020). The user's affiliation needs to belong to an ECMWF member state to benefit from these data sets. Due to restrictions on the input data sets for this simulation, the data can only be made available upon special request from the corresponding author.

Author Contributions

TS prepared all emission data, set up the model and performed the simulation supported by HSB. HSB reclassified the CORINE land use data set. KWS and TB conceived the idea and coordinated the project with VW. TS prepared all figures and wrote the manuscript with input from all authors. All authors equally contributed to the scientific discussion and helped to shape the research.

Video Supplement

The video shows the simulated diurnal evolution of the NO_2 concentration (Schwitalla, 2021a) and PM_{10} concentration (Schwitalla, 2021b) over the Stuttgart metropolitan area.

Competing interests

The authors declare that they have no conflict of interest.

Acknowledgements

This study has been performed within the EU-funded project *Open Forecast* (Action number 2017-DE-IA-0170). We acknowledge ECMWF for providing analysis data from the operational IFS and CAMS reanalysis. The Emissions of atmospheric Compounds and Compilation of Ancillary Data (ECCAD) system is acknowledged for providing the CAMS-REG-AP Emission data set. We acknowledge the use of the WRF-Chem preprocessor tool MOZBC, provided by the Atmospheric Chemistry Observations and Modeling Lab (ACOM) of NCAR. The Baden-Württemberg State Institute for the Environment (LUBW) is highly acknowledged for providing high-

resolution annual emission data and for the high-resolution land cover data. Joachim Ingwersen from the Department of Biogeophysics at the University of Hohenheim is acknowledged for converting the soil texture data. Joachim Fallmann from the University of Mainz is acknowledged for providing the necessary code enhancement of the dry deposition driver module to correctly couple the urban canopy model. The simulation was performed on the national supercomputer Cray XC40 Hazel Hen at the High Performance Computing Center Stuttgart (HLRS) within the WRFSCALE project. We acknowledge the editor Ronald Cohen and both anonymous referees for their valuable comments to improve the quality of the paper.

References

Ackermann, I. J., Hass, H., Memmesheimer, M., Ebel, A., Binkowski, F. S., and Shankar, U.: Modal aerosol dynamics model for Europe, Atmospheric Environment, 32, 2981–2999, https://doi.org/10.1016/S1352-2310(98)00006-5, 1998.

Baldauf, M., Seifert, A., Förstner, J., Majewski, D., Raschendorfer, M., and Reinhardt, T.: Operational Convective-Scale Numerical Weather Prediction with the COSMO Model: Description and Sensitivities, Mon. Wea. Rev., 139, 3887–3905, https://doi.org/10.1175/MWR-D-10-05013.1, 2011.

Barker, D., Huang, X.-Y., Liu, Z., Auligné, T., Zhang, X., Rugg, S., Ajjaji, R., Bourgeois, A., Bray, J., Chen, Y., Demirtas, M., Guo, Y.-R., Henderson, T., Huang, W., Lin, H.-C., Michalakes, J., Rizvi, S., and Zhang, X.: The Weather Research and Forecasting Model's Community Variational/Ensemble Data Assimilation System: WRFDA, Bull. Amer. Meteor. Soc., 93, 831–843, https://doi.org/10.1175/BAMS-D-11-00167.1, 2012.

Bauer, H.-S., Muppa, S. K., Wulfmeyer, V., Behrendt, A., Warrach-Sagi, K., and Späth, F.: Multi-nested WRF simulations for studying planetary boundary layer processes on the turbulence-permitting scale in a realistic mesoscale environment, Tellus A: Dynamic Meteorology and Oceanography, 72, 1–28, https://doi.org/10.1080/16000870.2020.1761740, 2020.

Bieser, J., Aulinger, A., Matthias, V., Quante, M., and van der Denier Gon, H. A. C.: Vertical emission profiles for Europe based on plume rise calculations, Environmental pollution (Barking, Essex 1987), 159, 2935–2946, https://doi.org/10.1016/j.envpol.2011.04.030, 2011.

Bonavita, M., Hólm, E., Isaksen, L., and Fisher, M.: The evolution of the ECMWF hybrid data assimilation system, Q.J.R. Meteorol. Soc., 142, 287–303, https://doi.org/10.1002/qj.2652, 2016.

Brasseur, G. P., Hauglustaine, D. A., Walters, S., Rasch, P. J., Müller, J.-F., Granier, C., and Tie, X. X.: MOZART, a global chemical transport model for ozone and related chemical tracers: 1. Model description, J. Geophys. Res., 103, 28265–28289, https://doi.org/10.1029/98JD02397, 1998.

Butcher, G., Barnes, C., and Owen, L.: Landsat: The cornerstone of global land imaging, GIM International, January/February 2019, 31–35, available at: http://pubs.er.usgs.gov/publication/70202363, 2019.

Chan, P. W.: Determination of Richardson number profile from remote sensing data and its aviation application, IOP Conf. Ser.: Earth Environ. Sci., 1, 12043, https://doi.org/10.1088/1755-1315/1/1/012043, 2008.

562 Chen, D., Liu, Z., Ban, J., Zhao, P., and Chen, M.: Retrospective analysis of 2015–2017
563 wintertime $PM_{2.5}$ in China: response to emission regulations and the role of meteorology,
564 Atmos. Chem. Phys., 19, 7409–7427, https://doi.org/10.5194/acp-19-7409-2019, 2019.
565 Copernicus: Copernicus official website, https://atmosphere.copernicus.eu/, last access: 21
566 July 2020.
567 Coppola, E., Sobolowski, S., Pichelli, E., Raffaele, F., Ahrens, B., Anders, I., Ban, N., Bastin, S.,
568 Belda, M., Belusic, D., Caldas-Alvarez, A., Cardoso, R. M., Davolio, S., Dobler, A.,
569 Fernandez, J., Fita, L., Fumiere, Q., Giorgi, F., Goergen, K., Güttler, I., Halenka, T.,
570 Heinzeller, D., Hodnebrog, Ø., Jacob, D., Kartsios, S., Katragkou, E., Kendon, E., Khodayar,
571 S., Kunstmann, H., Knist, S., Lavín-Gullón, A., Lind, P., Lorenz, T., Maraun, D., Marelle, L.,
572 van Meijgaard, E., Milovac, J., Myhre, G., Panitz, H.-J., Piazza, M., Raffa, M., Raub, T.,
573 Rockel, B., Schär, C., Sieck, K., Soares, P. M. M., Somot, S., Srnec, L., Stocchi, P., Tölle, M.
574 H., Truhetz, H., Vautard, R., Vries, H. de, and Warrach-Sagi, K.: A first-of-its-kind multi-
575 model convection permitting ensemble for investigating convective phenomena over
576 Europe and the Mediterranean, Clim Dyn, 55, 3–34, https://doi.org/10.1007/s00382-018-
577 4521-8, 2020.
578 Corsmeier, U., Kalthoff, N., Barthlott, C., Aoshima, F., Behrendt, A., Di Girolamo, P.,
579 Dorninger, M., Handwerker, J., Kottmeier, C., Mahlke, H., Mobbs, S. D., Norton, E. G.,
580 Wickert, J., and Wulfmeyer, V.: Processes driving deep convection over complex terrain:
581 a multi-scale analysis of observations from COPS IOP 9c, Q.J.R. Meteorol. Soc., 137, 137–
582 155, https://doi.org/10.1002/qj.754, 2011.
583 Danielson, J. J. and Gesch, D. B.: Global multi-resolution terrain elevation data 2010
584 (GMTED2010), Open-File report, 2011.
585 Denier van der Gon, H., Hendriks, C., Kuenen, J., Segers, A., and Visschedijk, A.: Description
586 of current temporal emission patterns and sensitivity of predicted AQ for temporal
587 emission patterns: EU FP7 MACC deliverable report D_D-EMIS_1.3, TNO report, 2011.
588 European Union: Copernicus Land Monitoring Service 2017, European Environment Agency,
589 2017.
590 European Union: Copernicus Land Monitoring Service 2012, European Environment Agency,
591 2012.
592 Fallmann, J.: Numerical simulations to assess the effect of urban heat island mitigation
593 strategies on regional air quality, PhD Thesis, Universität zu Köln, Cologne, 2014.
594 Fallmann, J., Forkel, R., and Emeis, S.: Secondary effects of urban heat island mitigation
595 measures on air quality, Atmospheric Environment, 125, 199–211,
596 https://doi.org/10.1016/j.atmosenv.2015.10.094, 2016.
597 Fallmann, J., Emeis, S., and Suppan, P.: Mitigation of urban heat stress – a modelling case
598 study for the area of Stuttgart, DIE ERDE – Journal of the Geographical Society of Berlin,
599 144, 202–216, https://doi.org/10.12854/erde-144-15, 2014.
600 Farr, T. G., Rosen, P. A., Caro, E., Crippen, R., Duren, R., Hensley, S., Kobrick, M., Paller, M.,
601 Rodriguez, E., Roth, L., Seal, D., Shaffer, S., Shimada, J., Umland, J., Werner, M., Oskin,
602 M., Burbank, D., and Alsdorf, D.: The Shuttle Radar Topography Mission, Rev. Geophys.,
603 45, https://doi.org/10.1029/2005RG000183, 2007.
604 Flemming, J., Huijnen, V., Arteta, J., Bechtold, P., Beljaars, A., Blechschmidt, A.-M.,
605 Diamantakis, M., Engelen, R. J., Gaudel, A., Inness, A., Jones, L., Josse, B., Katragkou, E.,

606 Marecal, V., Peuch, V.-H., Richter, A., Schultz, M. G., Stein, O., and Tsikerdekis, A.:
607 Tropospheric chemistry in the Integrated Forecasting System of ECMWF, Geosci. Model
608 Dev., 8, 975–1003, https://doi.org/10.5194/gmd-8-975-2015, 2015.
609 Forkel, R., Balzarini, A., Baró, R., Bianconi, R., Curci, G., Jiménez-Guerrero, P., Hirtl, M.,
610 Honzak, L., Lorenz, C., Im, U., Pérez, J. L., Pirovano, G., San José, R., Tuccella, P., Werhahn,
611 J., and Žabkar, R.: Analysis of the WRF-Chem contributions to AQMEII phase2 with
612 respect to aerosol radiative feedbacks on meteorology and pollutant distributions,
613 Atmospheric Environment, 115, 630–645,
614 https://doi.org/10.1016/j.atmosenv.2014.10.056, 2015.
615 Freitas, S. R., Longo, K. M., Alonso, M. F., Pirre, M., Marecal, V., Grell, G., Stockler, R., Mello,
616 R. F., and Sánchez Gácita, M.: PREP-CHEM-SRC – 1.0: a preprocessor of trace gas and
617 aerosol emission fields for regional and global atmospheric chemistry models, Geosci.
618 Model Dev., 4, 419–433, https://doi.org/10.5194/gmd-4-419-2011, 2011.
619 Freitas, S. R., Panetta, J., Longo, K. M., Rodrigues, L. F., Moreira, D. S., Rosário, N. E., Silva
620 Dias, P. L., Silva Dias, M. A. F., Souza, E. P., Freitas, E. D., Longo, M., Frassoni, A., Fazenda,
621 A. L., Santos e Silva, C. M., Pavani, C. A. B., Eiras, D., França, D. A., Massaru, D., Silva, F. B.,
622 Santos, F. C., Pereira, G., Camponogara, G., Ferrada, G. A., Campos Velho, H. F., Menezes,
623 I., Freire, J. L., Alonso, M. F., Gácita, M. S., Zarzur, M., Fonseca, R. M., Lima, R. S., Siqueira,
624 R. A., Braz, R., Tomita, S., Oliveira, V., and Martins, L. D.: The Brazilian developments on
625 the Regional Atmospheric Modeling System (BRAMS 5.2): an integrated environmental
626 model tuned for tropical areas, Geosci. Model Dev., 10, 189–222,
627 https://doi.org/10.5194/gmd-10-189-2017, 2017.
628 García-Díez, M., Lauwaet, D., Hooyberghs, H., Ballester, J., Ridder, K. de, and Rodó, X.:
629 Advantages of using a fast urban boundary layer model as compared to a full mesoscale
630 model to simulate the urban heat island of Barcelona, Geosci. Model Dev., 9, 4439–4450,
631 https://doi.org/10.5194/gmd-9-4439-2016, 2016.
632 Giorgi, F., Coppola, E., Solmon, F., Mariotti, L., Sylla, M. B., Bi, X., Elguindi, N., Diro, G. T.,
633 Nair, V., Giuliani, G., Turuncoglu, U. U., Cozzini, S., Güttler, I., O'Brien, T. A., Tawfik, A. B.,
634 Shalaby, A., Zakey, A. S., Steiner, A. L., Stordal, F., Sloan, L. C., and Brankovic, C.: RegCM4:
635 model description and preliminary tests over multiple CORDEX domains, Clim. Res., 52,
636 7–29, https://doi.org/10.3354/cr01018, 2012.
637 Glaser, K., Vogt, U., Baumbach, G., Volz-Thomas, A., and Geiss, H.: Vertical profiles of O 3 NO
638 2 NO x VOC, and meteorological parameters during the Berlin Ozone Experiment
639 (BERLIOZ) campaign, J. Geophys. Res., 108, https://doi.org/10.1029/2002JD002475,
640 available at: https://agupubs.onlinelibrary.wiley.com/doi/full/10.1029/2002JD002475,
641 2003.
642 Granier, C., Darras, S., Denier van der Gon, H., Doubalova, J., Elguindi, N., Galle, B., Gauss,
643 M., Guevara, M., Jalkanen, J.-P., Kuenen, J., Liousse, C., Quack, B., Simpson, D., and
644 Sindelarova, K.: The Copernicus Atmosphere Monitoring Service global and regional
645 emissions (April 2019 version), 2019.
646 Grell, G. A., Peckham, S. E., Schmitz, R., McKeen, S. A., Frost, G., Skamarock, W. C., and Eder,
647 B.: Fully coupled "online" chemistry within the WRF model, Atmospheric Environment,
648 39, 6957–6975, https://doi.org/10.1016/j.atmosenv.2005.04.027, 2005.

649 Guevara, M., Jorba, O., Tena, C., van der Denier Gon, H., Kuenen, J., Elguindi-Solmon, N.,
650 Darras, S., Granier, C., and Pérez García-Pando, C.: CAMS-TEMPO: global and European
651 emission temporal profile maps for atmospheric chemistry modelling, 2020.
652 Heinze, R., Moseley, C., Böske, L. N., Muppa, S. K., Maurer, V., Raasch, S., and Stevens, B.:
653 Evaluation of large-eddy simulations forced with mesoscale model output for a multi-
654 week period during a measurement campaign, Atmos. Chem. Phys., 17, 7083–7109,
655 https://doi.org/10.5194/acp-17-7083-2017, 2017a.
656 Heinze, R., Dipankar, A., Henken, C. C., Moseley, C., Sourdeval, O., Trömel, S., Xie, X.,
657 Adamidis, P., Ament, F., Baars, H., Barthlott, C., Behrendt, A., Blahak, U., Bley, S., Brdar,
658 S., Brueck, M., Crewell, S., Deneke, H., Di Girolamo, P., Evaristo, R., Fischer, J., Frank, C.,
659 Friederichs, P., Göcke, T., Gorges, K., Hande, L., Hanke, M., Hansen, A., Hege, H.-C.,
660 Hoose, C., Jahns, T., Kalthoff, N., Klocke, D., Kneifel, S., Knippertz, P., Kuhn, A., van Laar,
661 T., Macke, A., Maurer, V., Mayer, B., Meyer, C. I., Muppa, S. K., Neggers, R. A. J., Orlandi,
662 E., Pantillon, F., Pospichal, B., Röber, N., Scheck, L., Seifert, A., Seifert, P., Senf, F., Siligam,
663 P., Simmer, C., Steinke, S., Stevens, B., Wapler, K., Weniger, M., Wulfmeyer, V., Zängl, G.,
664 Zhang, D., and Quaas, J.: Large-eddy simulations over Germany using ICON: a
665 comprehensive evaluation, Q.J.R. Meteorol. Soc., 143, 69–100,
666 https://doi.org/10.1002/qj.2947, 2017b.
667 Hengl, T., Heuvelink, G. B. M., Kempen, B., Leenaars, J. G. B., Walsh, M. G., Shepherd, K. D.,
668 Sila, A., MacMillan, R. A., Mendes de Jesus, J., Tamene, L., and Tondoh, J. E.: Mapping Soil
669 Properties of Africa at 250 m Resolution: Random Forests Significantly Improve Current
670 Predictions, PloS one, 10, e0125814, https://doi.org/10.1371/journal.pone.0125814,
671 2015.
672 Hengl, T., Jesus, J. M. de, MacMillan, R. A., Batjes, N. H., Heuvelink, G. B. M., Ribeiro, E.,
673 Samuel-Rosa, A., Kempen, B., Leenaars, J. G. B., Walsh, M. G., and Gonzalez, M. R.:
674 SoilGrids1km--global soil information based on automated mapping, PloS one, 9,
675 e105992, https://doi.org/10.1371/journal.pone.0105992, 2014.
676 Hong, S.-Y., Noh, Y., and Dudhia, J.: A New Vertical Diffusion Package with an Explicit
677 Treatment of Entrainment Processes, Mon. Wea. Rev., 134, 2318–2341,
678 https://doi.org/10.1175/MWR3199.1, 2006.
679 Honnert, R. and Masson, V.: What is the smallest physically acceptable scale for 1D
680 turbulence schemes?, Front. Earth Sci., 2, 27, https://doi.org/10.3389/feart.2014.00027,
681 2014.
682 Honnert, R., Efstathiou, G. A., Beare, R. J., Ito, J., Lock, A., Neggers, R., Plant, R. S., Shin, H. H.,
683 Tomassini, L., and Zhou, B.: The Atmospheric Boundary Layer and the “Gray Zone” of
684 Turbulence: A Critical Review, J. Geophys. Res. Atmos., 125,
685 https://doi.org/10.1029/2019JD030317, 2020.
686 Horowitz, L. W., Walters, S., Mauzerall, D. L., Emmons, L. K., Rasch, P. J., Granier, C., Tie, X.,
687 Lamarque, J.-F., Schultz, M. G., Tyndall, G. S., Orlando, J. J., and Brasseur, G. P.: A global
688 simulation of tropospheric ozone and related tracers: Description and evaluation of
689 MOZART, version 2, J. Geophys. Res., 108, n/a-n/a,
690 https://doi.org/10.1029/2002JD002853, 2003.
691 Huszar, P., Karlický, J., Ďoubalová, J., Šindelářová, K., Nováková, T., Belda, M., Halenka, T.,
692 Žák, M., and Pišoft, P.: Urban canopy meteorological forcing and its impact on ozone and

$PM_{2.5}$: role of vertical turbulent transport, Atmos. Chem. Phys., 20, 1977–2016, https://doi.org/10.5194/acp-20-1977-2020, 2020.
Iacono, M. J., Delamere, J. S., Mlawer, E. J., Shephard, M. W., Clough, S. A., and Collins, W. D.: Radiative forcing by long-lived greenhouse gases: Calculations with the AER radiative transfer models, J. Geophys. Res., 113, https://doi.org/10.1029/2008JD009944, 2008.
Inness, A., Ades, M., Agustí-Panareda, A., Barré, J., Benedictow, A., Blechschmidt, A.-M., Dominguez, J. J., Engelen, R., Eskes, H., Flemming, J., Huijnen, V., Jones, L., Kipling, Z., Massart, S., Parrington, M., Peuch, V.-H., Razinger, M., Remy, S., Schulz, M., and Suttie, M.: The CAMS reanalysis of atmospheric composition, Atmos. Chem. Phys., 19, 3515–3556, https://doi.org/10.5194/acp-19-3515-2019, 2019.
Jiménez, P. A., Dudhia, J., González-Rouco, J. F., Navarro, J., Montávez, J. P., and García-Bustamante, E.: A Revised Scheme for the WRF Surface Layer Formulation, Mon. Wea. Rev., 140, 898–918, https://doi.org/10.1175/MWR-D-11-00056.1, 2012.
Jin, L., Li, Z., He, Q., Miao, Q., Zhang, H., and Yang, X.: Observation and simulation of near-surface wind and its variation with topography in Urumqi, West China, J Meteorol Res, 30, 961–982, https://doi.org/10.1007/s13351-016-6012-3, 2016.
Karlický, J., Huszár, P., Nováková, T., Belda, M., Švábik, F., Ďoubalová, J., and Halenka, T.: The `urban meteorology island': a multi-model ensemble analysis, 2020.
Kawabata, T., Schwitalla, T., Adachi, A., Bauer, H.-S., Wulfmeyer, V., Nagumo, N., and Yamauchi, H.: Observational operators for dual polarimetric radars in variational data assimilation systems (PolRad VAR v1.0), Geosci. Model Dev., 11, 2493–2501, https://doi.org/10.5194/gmd-11-2493-2018, 2018.
Kealy, J. C., Efstathiou, G. A., and Beare, R. J.: The Onset of Resolved Boundary-Layer Turbulence at Grey-Zone Resolutions, Boundary-Layer Meteorol, 171, 31–52, https://doi.org/10.1007/s10546-018-0420-0, 2019.
Khan, B., Banzhaf, S., Chan, E. C., Forkel, R., Kanani-Sühring, F., Ketelsen, K., Kurppa, M., Maronga, B., Mauder, M., Raasch, S., Russo, E., Schaap, M., and Sühring, M.: Development of an atmospheric chemistry model coupled to the PALM model system 6.0: Implementation and first applications, Geosci. Model Dev., https://doi.org/10.5194/gmd-2020-286, 2020.
Kosovic, B.: Subgrid-scale modelling for the large-eddy simulation of high-Reynolds-number boundary layers, J. Fluid Mech., 336, 151–182, https://doi.org/10.1017/S0022112096004697, 1997.
Kuenen, J. J. P., Visschedijk, A. J. H., Jozwicka, M., and van der Denier Gon, H. A. C.: TNO-MACC_II emission inventory; a multi-year (2003–2009) consistent high-resolution European emission inventory for air quality modelling, Atmos. Chem. Phys., 14, 10963–10976, https://doi.org/10.5194/acp-14-10963-2014, 2014.
Kuik, F., Kerschbaumer, A., Lauer, A., Lupascu, A., Schneidemesser, E. von, and Butler, T. M.: Top–down quantification of NO x emissions from traffic in an urban area using a high-resolution regional atmospheric chemistry model, Atmos. Chem. Phys., 18, 8203–8225, https://doi.org/10.5194/acp-18-8203-2018, 2018.
Kuik, F., Lauer, A., Churkina, G., van der Denier Gon, H. A. C., Fenner, D., Mar, K. A., and Butler, T. M.: Air quality modelling in the Berlin–Brandenburg region using WRF-Chem

v3.7.1: sensitivity to resolution of model grid and input data, Geosci. Model Dev., 9, 4339–4363, https://doi.org/10.5194/gmd-9-4339-2016, 2016.
Kusaka, H. and Kimura, F.: Coupling a Single-Layer Urban Canopy Model with a Simple Atmospheric Model: Impact on Urban Heat Island Simulation for an Idealized Case, JMSJ, 82, 67–80, https://doi.org/10.2151/jmsj.82.67, 2004.
Lee, T. R. and Wekker, S. F. J. de: Estimating Daytime Planetary Boundary Layer Heights over a Valley from Rawinsonde Observations at a Nearby Airport: An Application to the Page Valley in Virginia, United States, J. Appl. Meteor. Climatol., 55, 791–809, https://doi.org/10.1175/JAMC-D-15-0300.1, 2016.
Li, Z., Zhou, Y., Wan, B., Chung, H., Huang, B., and Liu, B.: Model evaluation of high-resolution urban climate simulations: using the WRF/Noah LSM/SLUCM model (Version 3.7.1) as a case study, Geosci. Model Dev., 12, 4571–4584, https://doi.org/10.5194/gmd-12-4571-2019, 2019.
Lin, D., Khan, B., Katurji, M., Bird, L., Faria, R., and Revell, L. E.: WRF4PALM v1.0: A Mesoscale Dynamical Driver for the Microscale PALM Model System 6.0, 2020.
Mailler, S., Menut, L., Khvorostyanov, D., Valari, M., Couvidat, F., Siour, G., Turquety, S., Briant, R., Tuccella, P., Bessagnet, B., Colette, A., Létinois, L., Markakis, K., and Meleux, F.: CHIMERE-2017: from urban to hemispheric chemistry-transport modeling, Geosci. Model Dev., 10, 2397–2423, https://doi.org/10.5194/gmd-10-2397-2017, 2017.
Manders, A. M. M., Builtjes, P. J. H., Curier, L., van der Denier Gon, H. A. C., Hendriks, C., Jonkers, S., Kranenburg, R., Kuenen, J. J. P., Segers, A. J., Timmermans, R. M. A., Visschedijk, A. J. H., Wichink Kruit, R. J., van Pul, W. A. J., Sauter, F. J., van der Swaluw, E., Swart, D. P. J., Douros, J., Eskes, H., van Meijgaard, E., van Ulft, B., van Velthoven, P., Banzhaf, S., Mues, A. C., Stern, R., Fu, G., Lu, S., Heemink, A., van Velzen, N., and Schaap, M.: Curriculum vitae of the LOTOS–EUROS (v2.0) chemistry transport model, Geosci. Model Dev., 10, 4145–4173, https://doi.org/10.5194/gmd-10-4145-2017, 2017.
Mar, K. A., Ojha, N., Pozzer, A., and Butler, T. M.: Ozone air quality simulations with WRF-Chem (v3.5.1) over Europe: model evaluation and chemical mechanism comparison, Geosci. Model Dev., 9, 3699–3728, https://doi.org/10.5194/gmd-9-3699-2016, 2016.
Marécal, V., Peuch, V.-H., Andersson, C., Andersson, S., Arteta, J., Beekmann, M., Benedictow, A., Bergström, R., Bessagnet, B., Cansado, A., Chéroux, F., Colette, A., Coman, A., Curier, R. L., van der Denier Gon, H. A. C., Drouin, A., Elbern, H., Emili, E., Engelen, R. J., Eskes, H. J., Foret, G., Friese, E., Gauss, M., Giannaros, C., Guth, J., Joly, M., Jaumouillé, E., Josse, B., Kadygrov, N., Kaiser, J. W., Krajsek, K., Kuenen, J., Kumar, U., Liora, N., Lopez, E., Malherbe, L., Martinez, I., Melas, D., Meleux, F., Menut, L., Moinat, P., Morales, T., Parmentier, J., Piacentini, A., Plu, M., Poupkou, A., Queguiner, S., Robertson, L., Rouïl, L., Schaap, M., Segers, A., Sofiev, M., Tarasson, L., Thomas, M., Timmermans, R., Valdebenito, Á., van Velthoven, P., van Versendaal, R., Vira, J., and Ung, A.: A regional air quality forecasting system over Europe: the MACC-II daily ensemble production, Geosci. Model Dev., 8, 2777–2813, https://doi.org/10.5194/gmd-8-2777-2015, 2015.
Maronga, B., Gryschka, M., Heinze, R., Hoffmann, F., Kanani-Sühring, F., Keck, M., Ketelsen, K., Letzel, M. O., Sühring, M., and Raasch, S.: The Parallelized Large-Eddy Simulation Model (PALM) version 4.0 for atmospheric and oceanic flows: model formulation, recent

developments, and future perspectives, Geosci. Model Dev., 8, 2515–2551, https://doi.org/10.5194/gmd-8-2515-2015, 2015.
Maronga, B., Banzhaf, S., Burmeister, C., Esch, T., Forkel, R., Fröhlich, D., Fuka, V., Gehrke, K. F., Geletič, J., Giersch, S., Gronemeier, T., Groß, G., Heldens, W., Hellsten, A., Hoffmann, F., Inagaki, A., Kadasch, E., Kanani-Sühring, F., Ketelsen, K., Khan, B. A., Knigge, C., Knoop, H., Krč, P., Kurppa, M., Maamari, H., Matzarakis, A., Mauder, M., Pallasch, M., Pavlik, D., Pfafferott, J., Resler, J., Rissmann, S., Russo, E., Salim, M., Schrempf, M., Schwenkel, J., Seckmeyer, G., Schubert, S., Sühring, M., Tils, R. von, Vollmer, L., Ward, S., Witha, B., Wurps, H., Zeidler, J., and Raasch, S.: Overview of the PALM model system 6.0, Geosci. Model Dev., 13, 1335–1372, https://doi.org/10.5194/gmd-13-1335-2020, 2020.
Maronga, B., Gross, G., Raasch, S., Banzhaf, S., Forkel, R., Heldens, W., Kanani-Sühring, F., Matzarakis, A., Mauder, M., Pavlik, D., Pfafferott, J., Schubert, S., Seckmeyer, G., Sieker, H., and Winderlich, K.: Development of a new urban climate model based on the model PALM – Project overview, planned work, and first achievements, metz, 28, 105–119, https://doi.org/10.1127/metz/2019/0909, 2019.
Marsh, D. R., Mills, M. J., Kinnison, D. E., Lamarque, J.-F., Calvo, N., and Polvani, L. M.: Climate Change from 1850 to 2005 Simulated in CESM1(WACCM), J. Climate, 26, 7372–7391, https://doi.org/10.1175/JCLI-D-12-00558.1, 2013.
Martilli, A., Clappier, A., and Rotach, M. W.: An Urban Surface Exchange Parameterisation for Mesoscale Models, Boundary-Layer Meteorology, 104, 261–304, https://doi.org/10.1023/A:1016099921195, 2002.
Memmesheimer, M., Friese, E., Ebel, A., Jakobs, H. J., Feldmann, H., Kessler, C., and Piekorz, G.: Long-term simulations of particulate matter in Europe on different scales using sequential nesting of a regional model, IJEP, 22, 108, https://doi.org/10.1504/IJEP.2004.005530, 2004.
Nakayama, H., Takemi, T., and Nagai, H.: Large-eddy simulation of urban boundary-layer flows by generating turbulent inflows from mesoscale meteorological simulations, Atmosph. Sci. Lett., 13, 180–186, https://doi.org/10.1002/asl.377, 2012.
Niu, G.-Y., Yang, Z.-L., Mitchell, K. E., Chen, F., Ek, M. B., Barlage, M., Kumar, A., Manning, K., Niyogi, D., Rosero, E., Tewari, M., and Xia, Y.: The community Noah land surface model with multiparameterization options (Noah-MP): 1. Model description and evaluation with local-scale measurements, J. Geophys. Res., 116, https://doi.org/10.1029/2010JD015139, 2011.
Panosetti, D., Böing, S., Schlemmer, L., and Schmidli, J.: Idealized Large-Eddy and Convection-Resolving Simulations of Moist Convection over Mountainous Terrain, J. Atmos. Sci., 73, 4021–4041, https://doi.org/10.1175/JAS-D-15-0341.1, 2016.
Pfister, G. G., Parrish, D. D., Worden, H., Emmons, L. K., Edwards, D. P., Wiedinmyer, C., Diskin, G. S., Huey, G., Oltmans, S. J., Thouret, V., Weinheimer, A., and Wisthaler, A.: Characterizing summertime chemical boundary conditions for airmasses entering the US West Coast, Atmos. Chem. Phys., 11, 1769–1790, https://doi.org/10.5194/acp-11-1769-2011, 2011.
Prein, A. F., Langhans, W., Fosser, G., Ferrone, A., Ban, N., Goergen, K., Keller, M., Tölle, M., Gutjahr, O., Feser, F., Brisson, E., Kollet, S., Schmidli, J., van Lipzig, N. P. M., and Leung, R.: A review on regional convection-permitting climate modeling: Demonstrations,

824 prospects, and challenges, Rev. Geophys., 53, 323–361,
825 https://doi.org/10.1002/2014RG000475, 2015.
826 Resler, J., Eben, K., Geletič, J., Krč, P., Rosecký, M., Sühring, M., Belda, M., Fuka, V., Halenka,
827 T., Huszár, P., Karlický, J., Benešová, N., Ďoubalová, J., Honzáková, K., Keder, J.,
828 Nápravníková, Š., and Vlček, O.: Validation of the PALM model system 6.0 in real urban
829 environment; case study of Prague-Dejvice, Czech Republic, Geosci. Model Dev.,
830 https://doi.org/10.5194/gmd-2020-175, 2020, under review.
831 Rieger, D., Bangert, M., Bischoff-Gauss, I., Förstner, J., Lundgren, K., Reinert, D., Schröter, J.,
832 Vogel, H., Zängl, G., Ruhnke, R., and Vogel, B.: ICON–ART 1.0 – a new online-coupled
833 model system from the global to regional scale, Geosci. Model Dev., 8, 1659–1676,
834 https://doi.org/10.5194/gmd-8-1659-2015, 2015.
835 Salamanca, F. and Martilli, A.: A new Building Energy Model coupled with an Urban Canopy
836 Parameterization for urban climate simulations—part II. Validation with one dimension
837 off-line simulations, Theor Appl Climatol, 99, 345–356, https://doi.org/10.1007/s00704-
838 009-0143-8, 2010.
839 Samad, A., Vogt, U., Panta, A., and Uprety, D.: Vertical distribution of particulate matter,
840 black carbon and ultra-fine particles in Stuttgart, Germany, Atmospheric Pollution
841 Research, 11, 1441–1450, https://doi.org/10.1016/j.apr.2020.05.017, 2020.
842 Schell, B., Ackermann, I. J., Hass, H., Binkowski, F. S., and Ebel, A.: Modeling the formation of
843 secondary organic aerosol within a comprehensive air quality model system, J. Geophys.
844 Res., 106, 28275–28293, https://doi.org/10.1029/2001JD000384, 2001.
845 Scherer, D., Antretter, F., Bender, S., Cortekar, J., Emeis, S., Fehrenbach, U., Gross, G., Halbig,
846 G., Hasse, J., Maronga, B., Raasch, S., and Scherber, K.: Urban Climate Under Change
847 [UC]2 – A National Research Programme for Developing a Building-Resolving
848 Atmospheric Model for Entire City Regions, metz, 28, 95–104,
849 https://doi.org/10.1127/metz/2019/0913, 2019.
850 Schwitalla, T.: Simulation of NO2 concentration over the Stuttgart metropolitan area, TIB AV-
851 Portal, https://doi.org/10.5446/50923, 2021a.
852 Schwitalla, T.: Simulation of PM10 concentration over the Stuttgart metropolitan area, TIB
853 AV-Portal, https://doi.org/10.5446/50924, 2021b.
854 Seidel, D. J., Zhang, Y., Beljaars, A., Golaz, J.-C., Jacobson, A. R., and Medeiros, B.:
855 Climatology of the planetary boundary layer over the continental United States and
856 Europe, J. Geophys. Res., 117, n/a-n/a, https://doi.org/10.1029/2012JD018143, 2012.
857 Skamarock, W. C., Klemp, J. B., Dudhia, J., Gill, D. O., Liu, Z., Berner, J., Wang, W., Powers, J.
858 G., Duda, M. G., Barker, D. M., and Huang, X.-Y.: A Description of the Advanced Research
859 WRF Model Version 4, 2019.
860 Steeneveld, G. J., Ronda, R. J., and Holtslag, A. A. M.: The Challenge of Forecasting the Onset
861 and Development of Radiation Fog Using Mesoscale Atmospheric Models, Boundary-
862 Layer Meteorol, 154, 265–289, https://doi.org/10.1007/s10546-014-9973-8, 2015.
863 Stockwell, W. R., Middleton, P., Chang, J. S., and Tang, X.: The second generation regional
864 acid deposition model chemical mechanism for regional air quality modeling, J. Geophys.
865 Res., 95, 16343, https://doi.org/10.1029/JD095iD10p16343, 1990.

Stuttgart Municipality and German Meteorological Service (DWD): Requirements for fine dust situations, https://feinstaubalarm.stuttgart.de/img/mdb/item/584405/119353.pdf, last access: 20 August 2020, 2019.
Sun, W., Liu, Z., Chen, D., Zhao, P., and Chen, M.: Development and application of the WRFDA-Chem three-dimensional variational (3DVAR) system: aiming to improve air quality forecasting and diagnose model deficiencies, Atmos. Chem. Phys., 20, 9311–9329, https://doi.org/10.5194/acp-20-9311-2020, 2020.
Teixeira, J. C., Fallmann, J., Carvalho, A. C., and Rocha, A.: Surface to boundary layer coupling in the urban area of Lisbon comparing different urban canopy models in WRF, Urban Climate, 28, 100454, https://doi.org/10.1016/j.uclim.2019.100454, 2019.
Thompson, G., Field, P. R., Rasmussen, R. M., and Hall, W. D.: Explicit Forecasts of Winter Precipitation Using an Improved Bulk Microphysics Scheme. Part II: Implementation of a New Snow Parameterization, Mon. Wea. Rev., 136, 5095–5115, https://doi.org/10.1175/2008MWR2387.1, 2008.
Thundathil, R., Schwitalla, T., Behrendt, A., Muppa, S. K., ADAM, S., and Wulfmeyer, V.: Assimilation of Lidar Water Vapour Mixing Ratio and Temperature Profiles into a Convection-Permitting Model, JMSJ, https://doi.org/10.2151/jmsj.2020-049, 2020.
Thunis, P., Degraeuwe, B., Pisoni, E., Trombetti, M., Peduzzi, E., Belis, C. A., Wilson, J., and Vignati, E.: Urban PM2.5 atlas: Air quality in European cities, JRC science for policy report, 28804, Publications Office, Luxembourg, 1 online resource, 2017.
UN: The World's Cities in 2018, United Nations, 2018.
Valcke, S., Balaji, V., Craig, A., DeLuca, C., Dunlap, R., Ford, R. W., Jacob, R., Larson, J., O'Kuinghttons, R., Riley, G. D., and Vertenstein, M.: Coupling technologies for Earth System Modelling, Geosci. Model Dev., 5, 1589–1596, https://doi.org/10.5194/gmd-5-1589-2012, 2012.
Vogel, B., Vogel, H., Bäumer, D., Bangert, M., Lundgren, K., Rinke, R., and Stanelle, T.: The comprehensive model system COSMO-ART – Radiative impact of aerosol on the state of the atmosphere on the regional scale, Atmos. Chem. Phys., 9, 8661–8680, https://doi.org/10.5194/acp-9-8661-2009, 2009.
Wang, D., Stachlewska, I. S., Song, X., Heese, B., and Nemuc, A.: Variability of the Boundary Layer Over an Urban Continental Site Based on 10 Years of Active Remote Sensing Observations in Warsaw, Remote Sensing, 12, 340, https://doi.org/10.3390/rs12020340, 2020.
WHO: WHO Air quality guidelines for particulate matter, ozone, nitrogen dioxide and sulfur dioxide. Global update 2005., 2005.
Yang, Z.-L., Niu, G.-Y., Mitchell, K. E., Chen, F., Ek, M. B., Barlage, M., Longuevergne, L., Manning, K., Niyogi, D., Tewari, M., and Xia, Y.: The community Noah land surface model with multiparameterization options (Noah-MP): 2. Evaluation over global river basins, J. Geophys. Res., 116, https://doi.org/10.1029/2010JD015140, 2011.
Zängl, G., Reinert, D., Rípodas, P., and Baldauf, M.: The ICON (ICOsahedral Non-hydrostatic) modelling framework of DWD and MPI-M: Description of the non-hydrostatic dynamical core, Q.J.R. Meteorol. Soc., 141, 563–579, https://doi.org/10.1002/qj.2378, 2015.
Zhang, X., Huang, X.-Y., Liu, J., Poterjoy, J., Weng, Y., Zhang, F., and Wang, H.: Development of an Efficient Regional Four-Dimensional Variational Data Assimilation System for WRF,

910 Journal of Atmospheric and Oceanic Technology, 31, 2777–2794,
911 https://doi.org/10.1175/JTECH-D-13-00076.1, 2014.
912 Zhong, M., Saikawa, E., Liu, Y., Naik, V., Horowitz, L. W., Takigawa, M., Zhao, Y., Lin, N.-H.,
913 and Stone, E. A.: Air quality modeling with WRF-Chem v3.5 in East Asia: sensitivity to
914 emissions and evaluation of simulated air quality, Geosci. Model Dev., 9, 1201–1218,
915 https://doi.org/10.5194/gmd-9-1201-2016, 2016.
916 Zieliński, M., Fortuniak, K., Pawlak, W., and Siedlecki, M.: Long-term Turbulent Sensible-
917 Heat-Flux Measurements with a Large-Aperture Scintillometer in the Centre of Łódź,
918 Central Poland, Boundary-Layer Meteorol, 167, 469–492,
919 https://doi.org/10.1007/s10546-017-0331-5, 2018.
920

921

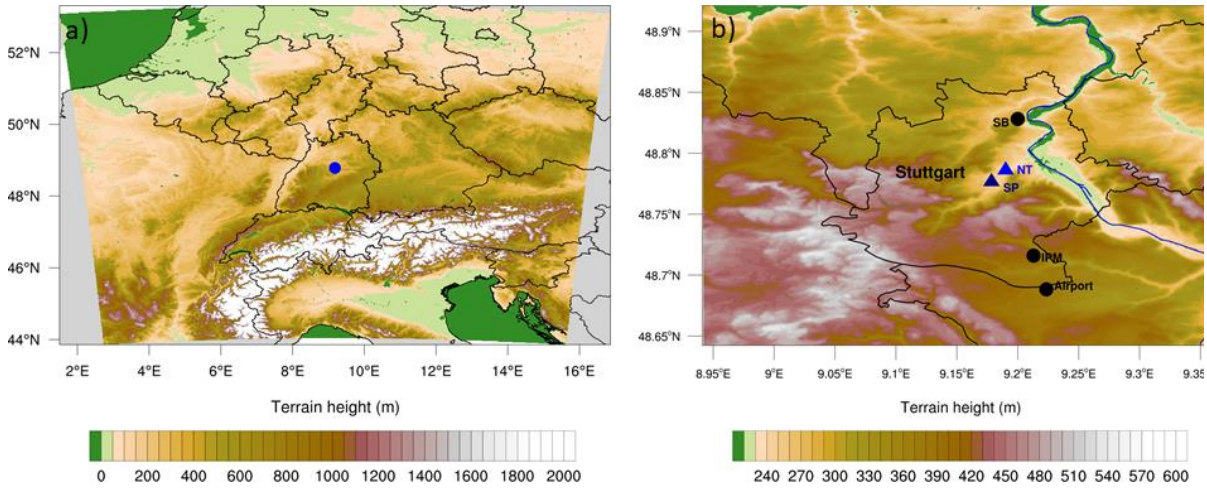

Figure 1: Model domain 1 (a) and domain 3 (b). The blue dot in (a) denotes Stuttgart. Black dots in (b) show the location of the meteorological measurement sites. The diamonds in (b) denotes the Neckartor (NT) and Schlossplatz (SP) locations and the blue contour line denotes the Neckar River (River data © OpenStreetMap contributors 2020. Distributed under a Creative Commons BY-SA License).

922

923

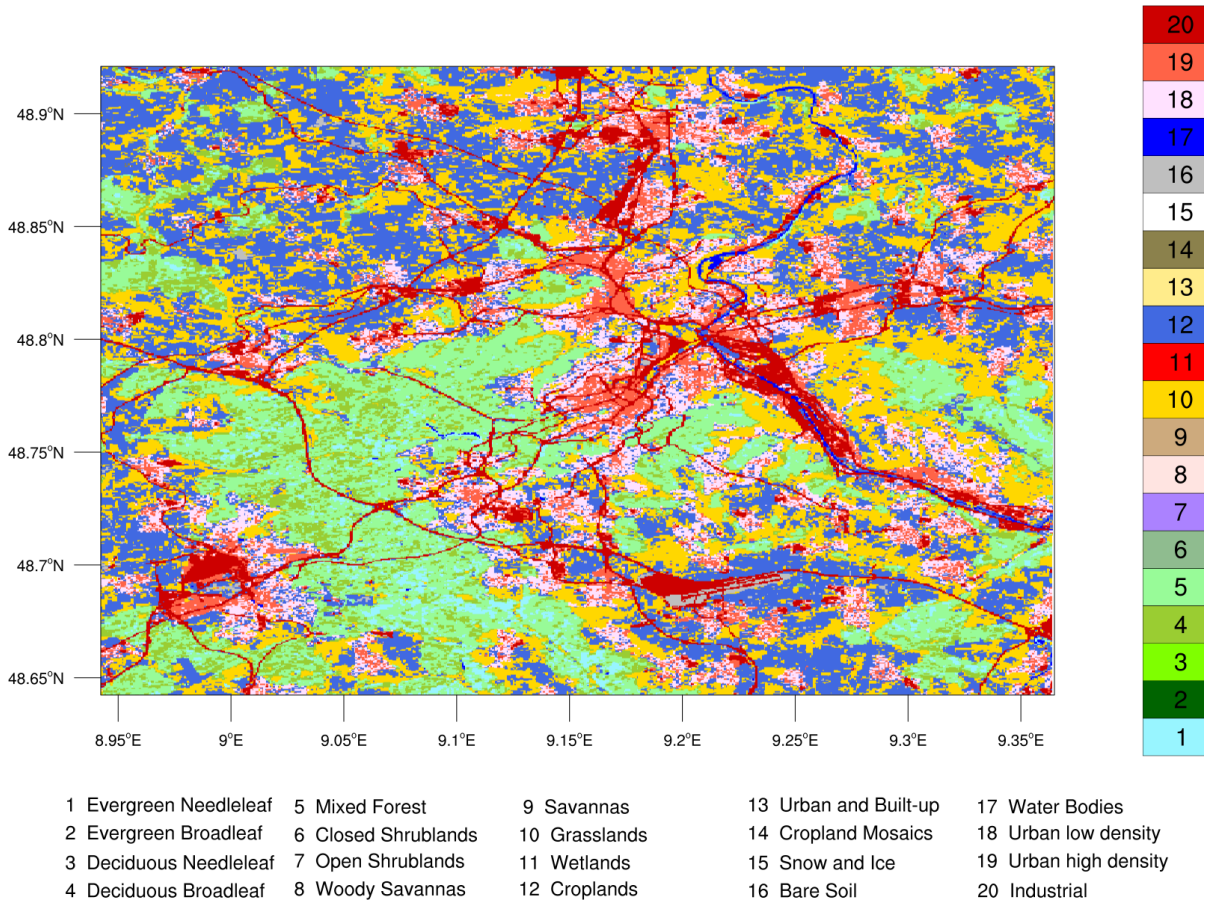

Figure 2: Land cover data from the Baden-Württemberg State Institute for the Environment (LUBW) reclassified for WRF in the innermost domain at a resolution of 50 m.

924

925

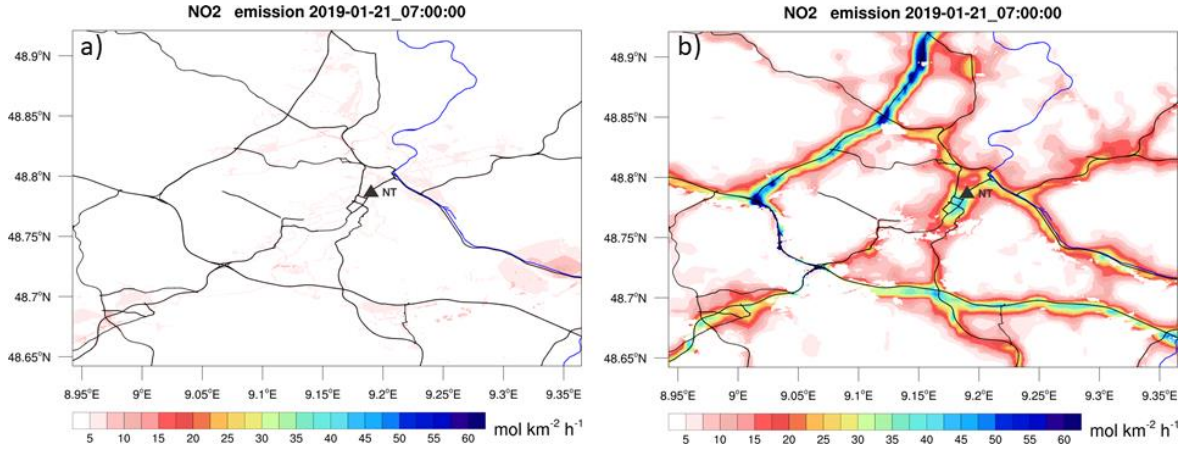

Figure 3: NO_2 emissions valid at 07 UTC on January 21, 2019. (a) shows the emissions derived from the CAMS-REG-AP data set and (b) shows the emissions derived from the BW-EMISS data set (Map Data © OpenStreetMap contributors 2020. Distributed under a Creative Commons BY-SA License).

926

927

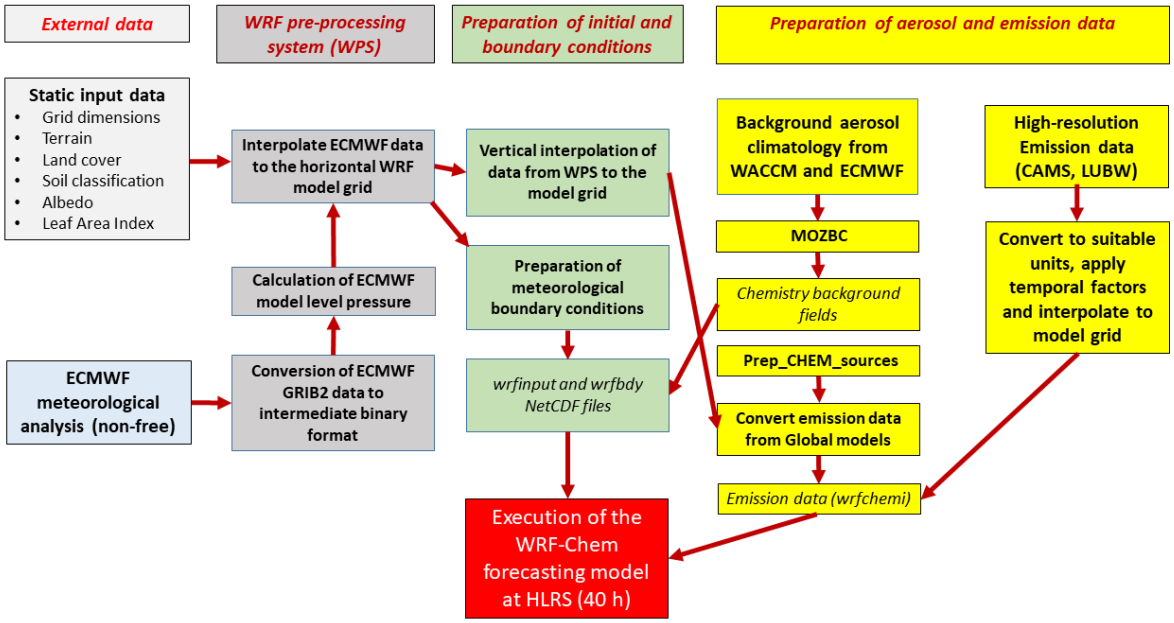

Figure 4: Workflow of the AQFS prototype system.

928

929

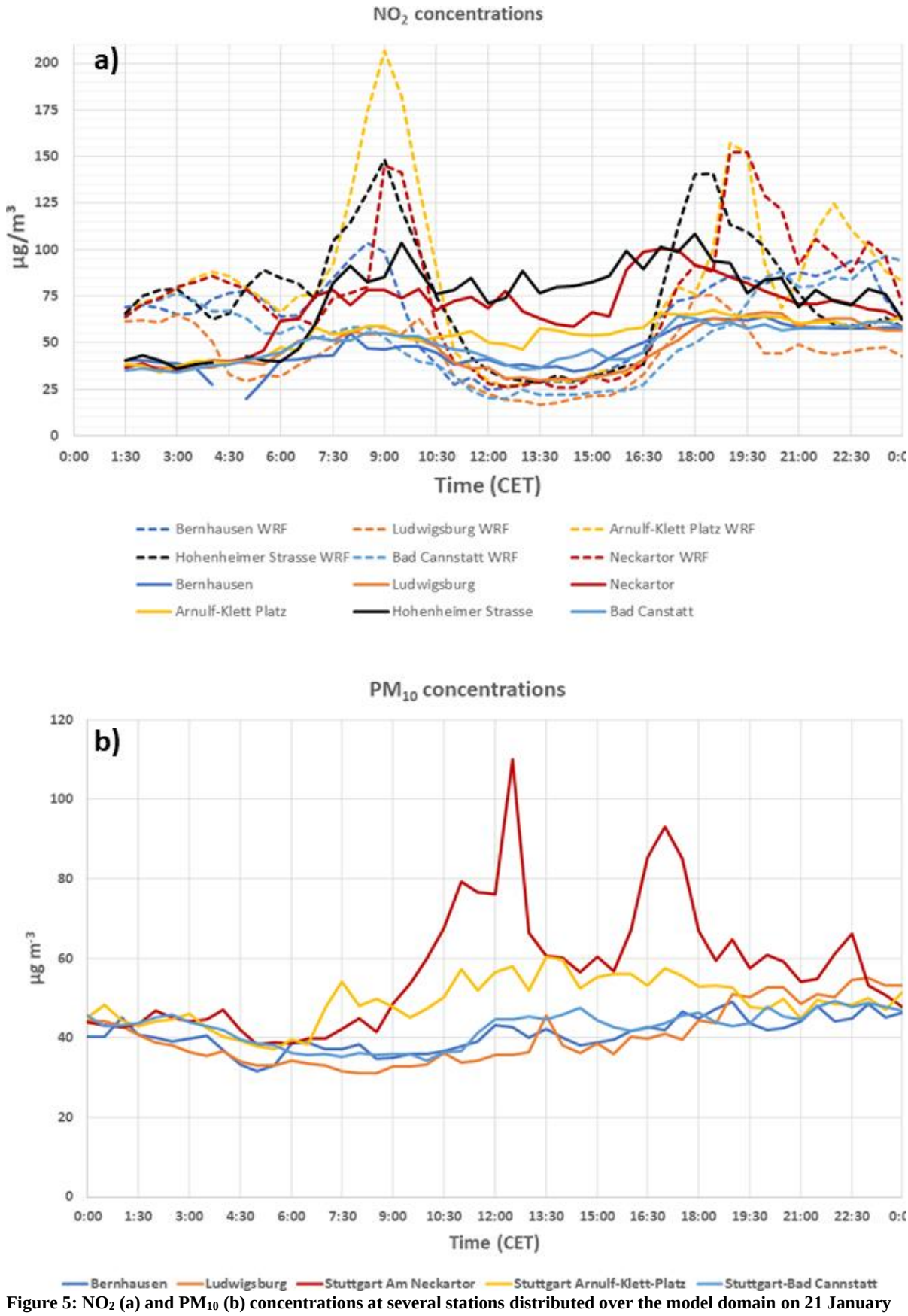

Figure 5: NO_2 (a) and PM_{10} (b) concentrations at several stations distributed over the model domain on 21 January 2019. The dashed line in (a) denotes the simulated NO_2 concentration and the time zone (CET) corresponds to local time. Measurements at Neckartor, Hohenheimer Strasse, and Arnulf-Klett Platz are directly taken next to the main road.

930

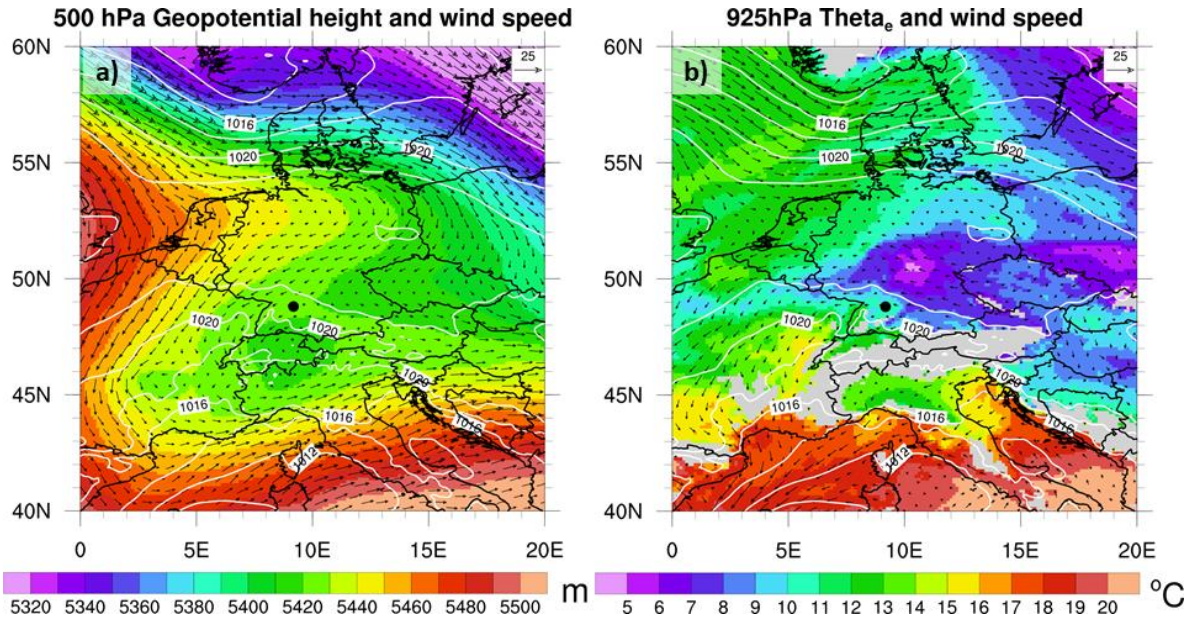

Figure 6: (a) ECMWF operational analysis of 500 hPa geopotential height, sea level pressure (white contour lines) together with 500 hPa wind velocities valid at 00 UTC 21 January 2019. (b) shows the 925hPa equivalent potential temperature together with 925 hPa wind velocities and sea level pressure (white contour lines). Gray areas indicate values below the ECMWF model terrain. The black dot denotes Stuttgart and the reference wind vector length (top right corner of each Figure)) is equal to 25 m s^{-1}.

931

932

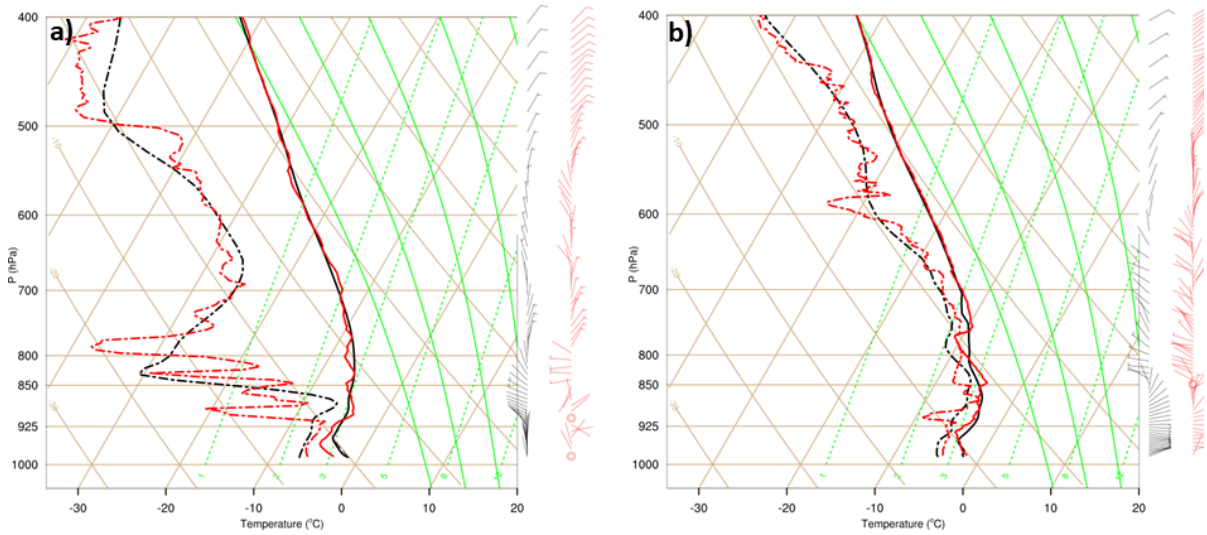

Figure 7: Comparison of temperature, dewpoint and wind of the WRF model simulation (black line) and the sounding from Stuttgart-Schnarrenberg (red line) valid at 00 UTC (a) and 11 UTC (b) 21 January 2019.The solid lines denote the temperature profile and the dash-dotted line denotes the dewpoint profile. Wind barbs denote wind speed in m s^{-1}.

933

934

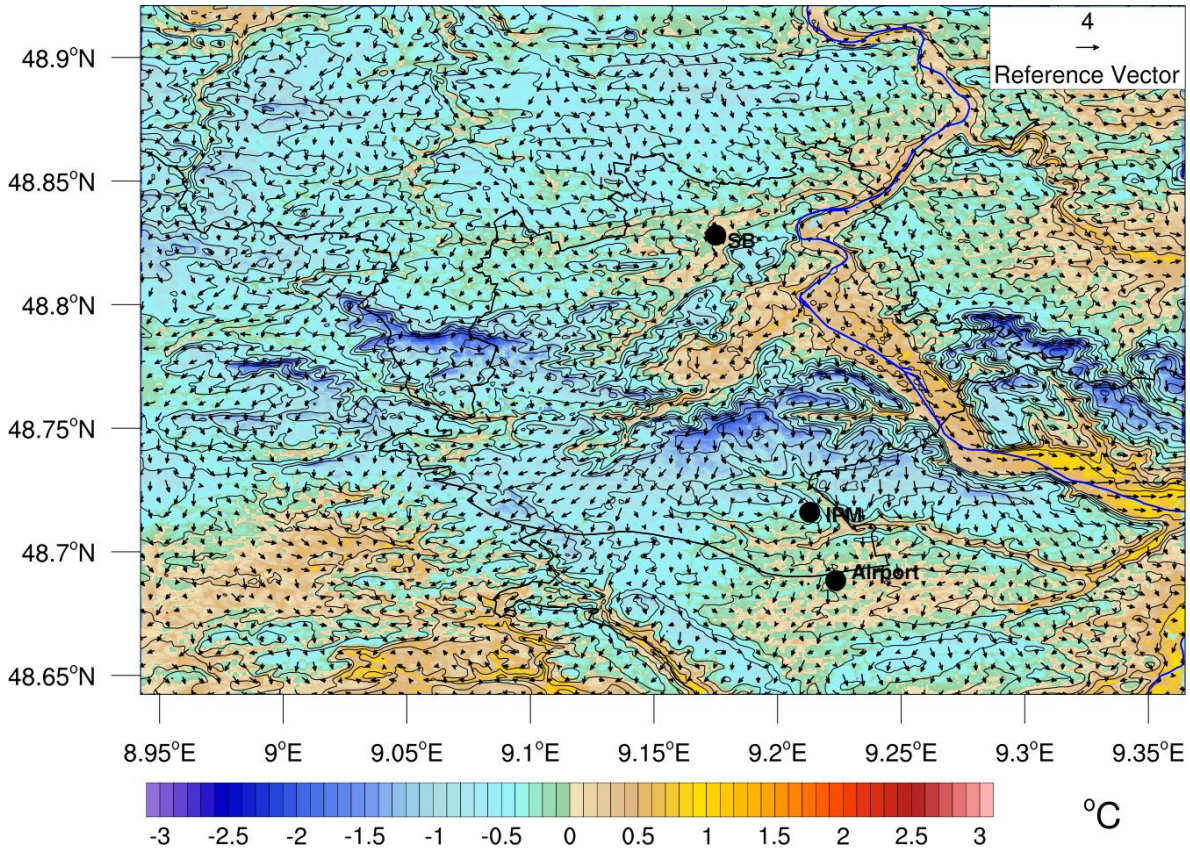

Figure 8: 2-m temperature together with 10-m wind velocities at 12 UTC 21 January 2019. The thick black line denotes the Stuttgart city limits and the thin black contour lines denote the terrain. The blue line denotes the Neckar River (River data © OpenStreetMap contributors 2020. Distributed under a Creative Commons BY-SA License).

935

936

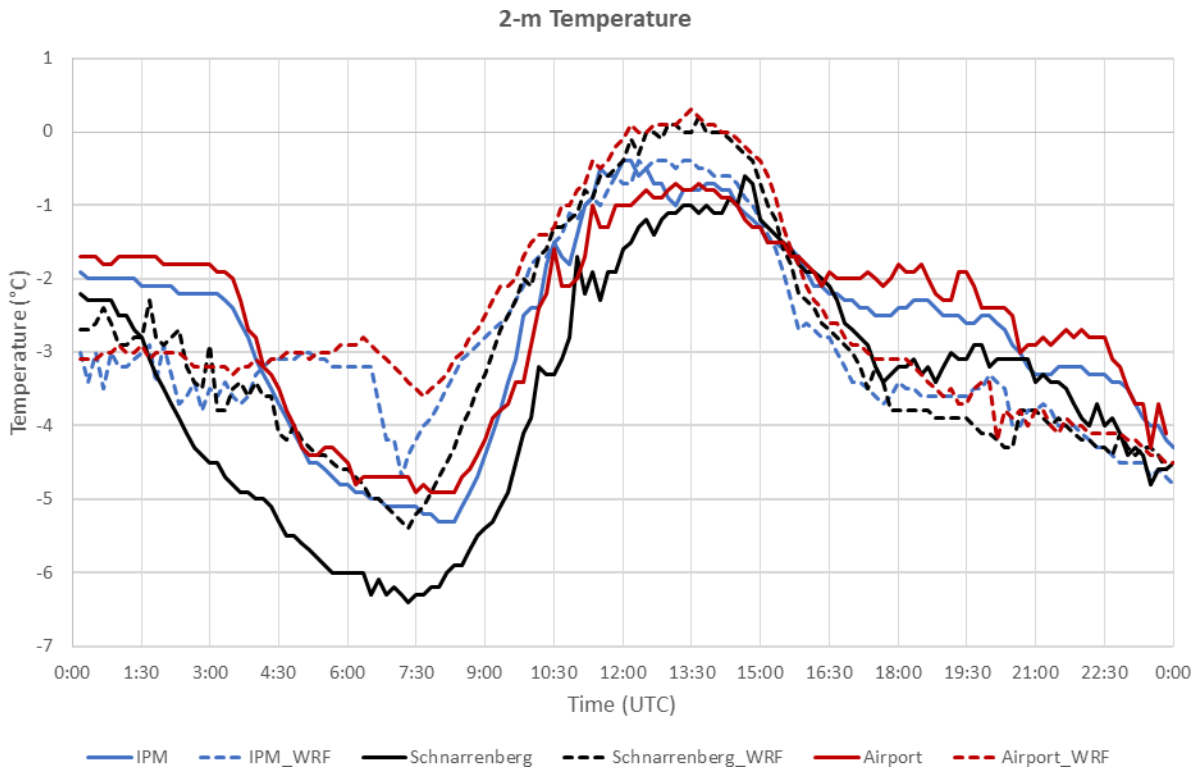

Figure 9: Diurnal cycle of 2-m temperatures for the three meteorological stations shown in Fig. 1b. Solid lines denote the observation, dashed lines denote the model simulation. The temporal resolution of the data points is 10 minutes.

937

938

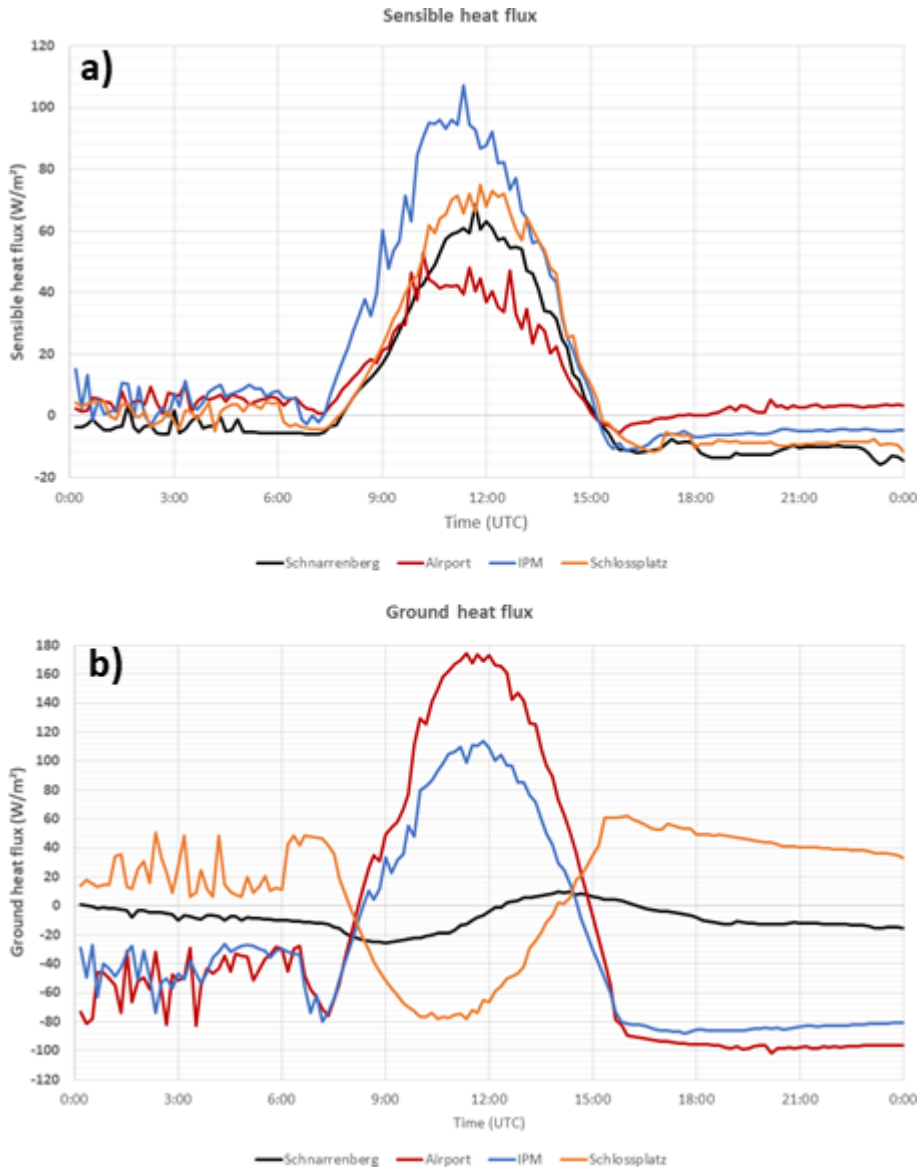

Figure 10: Diurnal cycle of simulated sensible heat flux (SH, a) and ground heat flux (GRDFLX, b) at the four stations Schnarrenberg, Airport, IPM, and Schlossplatz (Fig. 1b). Positive values of GRDFLX indicate fluxes into the soil. The land cover categories are bare soil (airport), croplands (IPM), low-density residential (Schnarrenberg), and high-density residential (Schlossplatz).

939

940

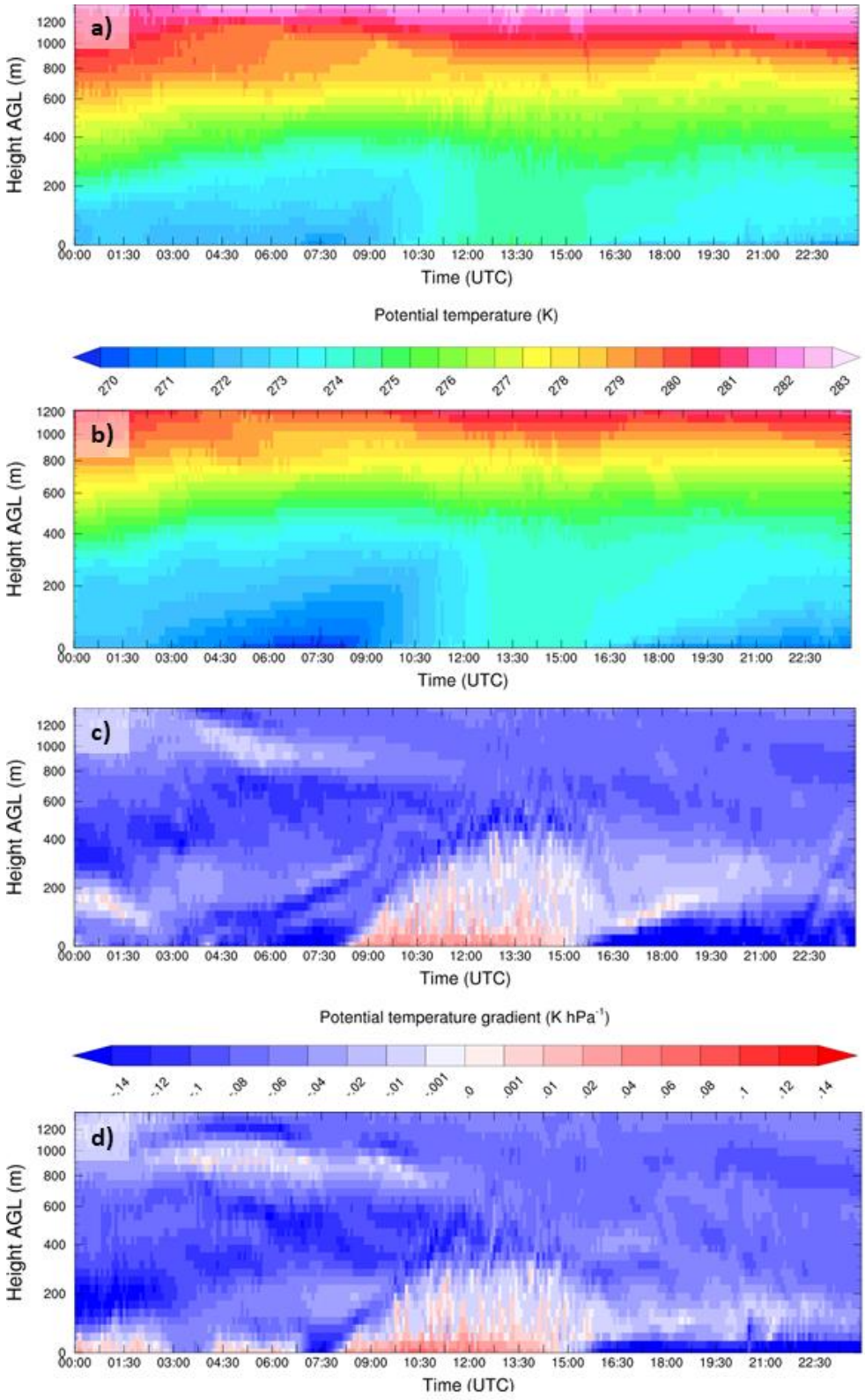

Figure 11: Time-height cross section of the simulated potential temperature at Schnarrenberg (a) and IPM (b). (c) and (d) show the potential temperature gradient at Schnarrenberg (c) and IPM (d).The displayed altitude is above ground level (AGL).

941

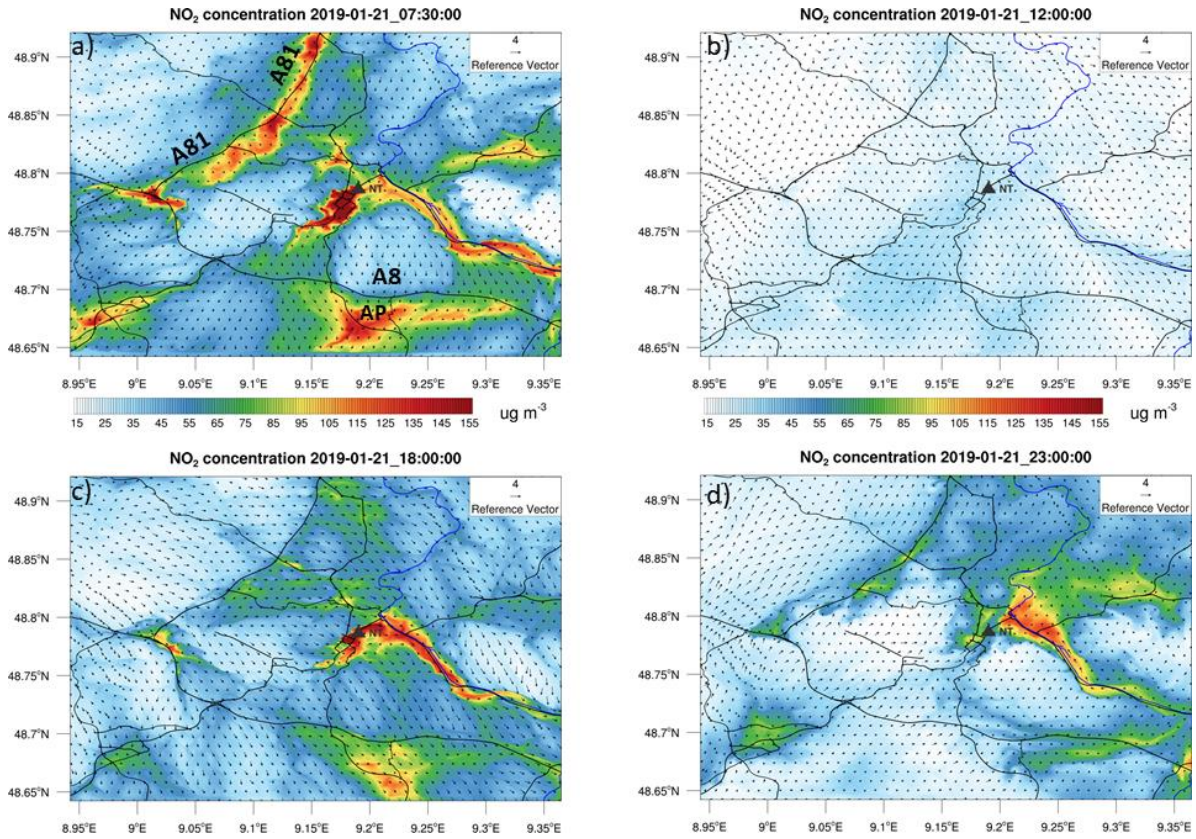

Figure 12: NO_2 concentration at the lowest model level for 07:30 UTC, 12 UTC, 18:00 UTC, and 23 UTC (from a to d) 21 January 2019. The black contour lines denote main roads and motorways in and around Stuttgart (Map Data © OpenStreetMap contributors 2020. Distributed under a Creative Commons BY-SA License). AP denotes the airport, A8 and A81 denote the main motorways around Stuttgart.

942

943

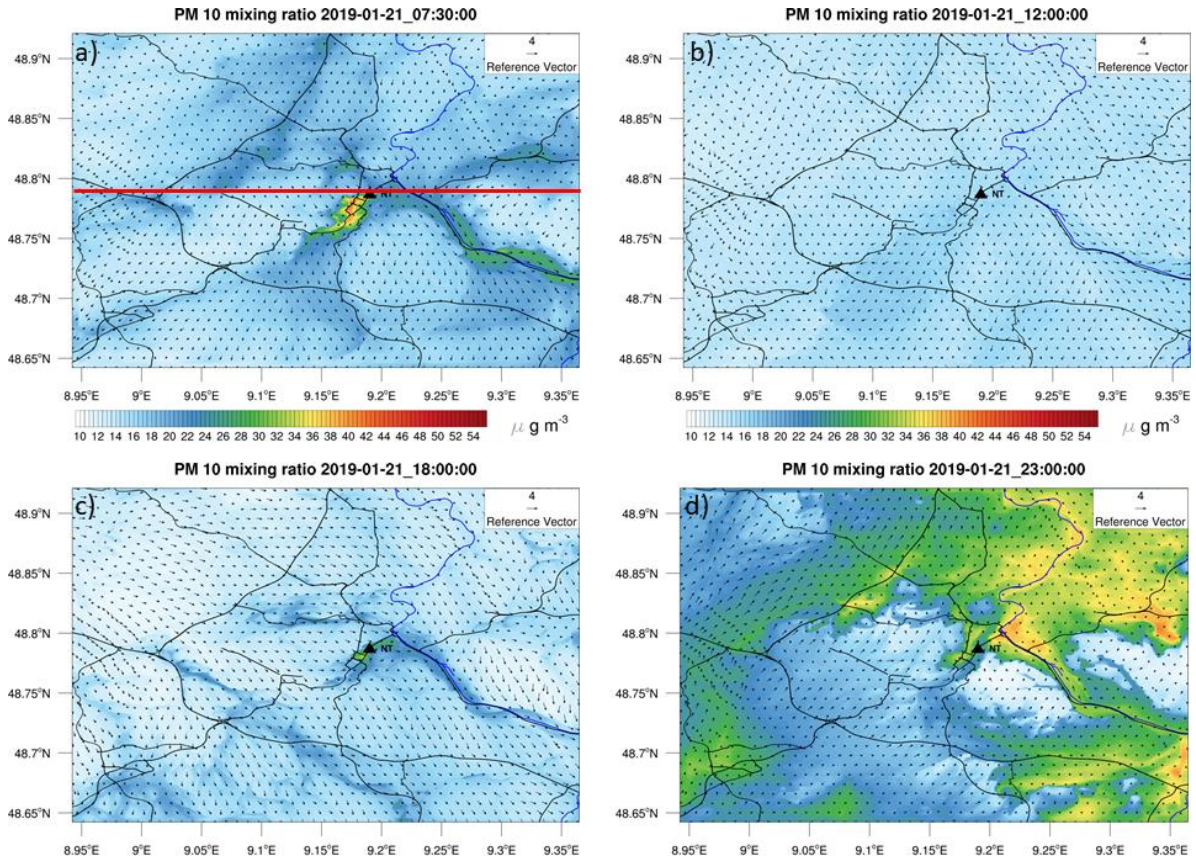

Figure 13: Same as Fig. 12 but for PM_{10} (Map Data © OpenStreetMap contributors 2020. Distributed under a Creative Commons BY-SA License). The red line in (a) denotes the cross section shown in Figs. 14 and 15.

944

945

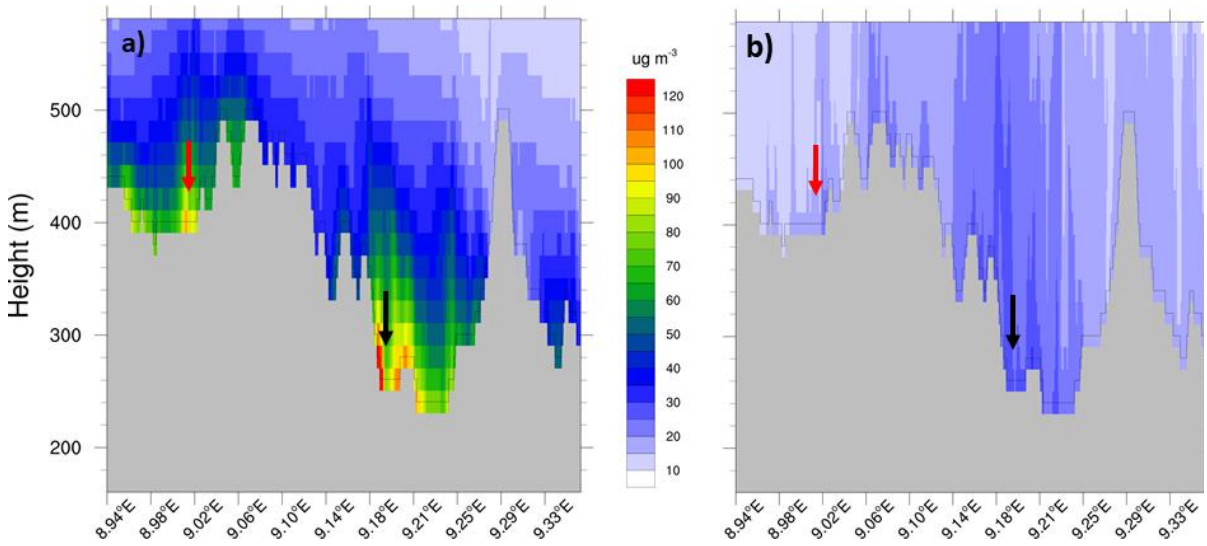

Figure 14: West-East cross section through Neckartor displaying the NO_2 concentration at 07:30 UTC (a) and 12 UTC (b), 21 January 2019. The red arrow denotes the motorway A81 and the black arrow denotes the Neckartor location. The black area shows the model terrain above mean sea level.

946

947

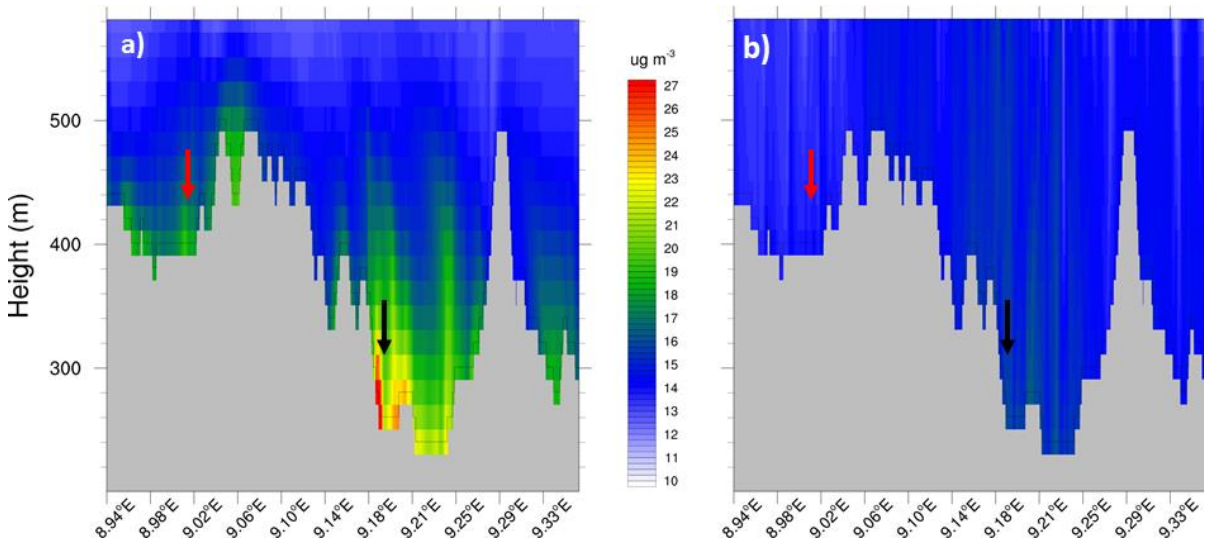

Figure 15: Same as Fig. 14 but for PM_{10}.

948

949

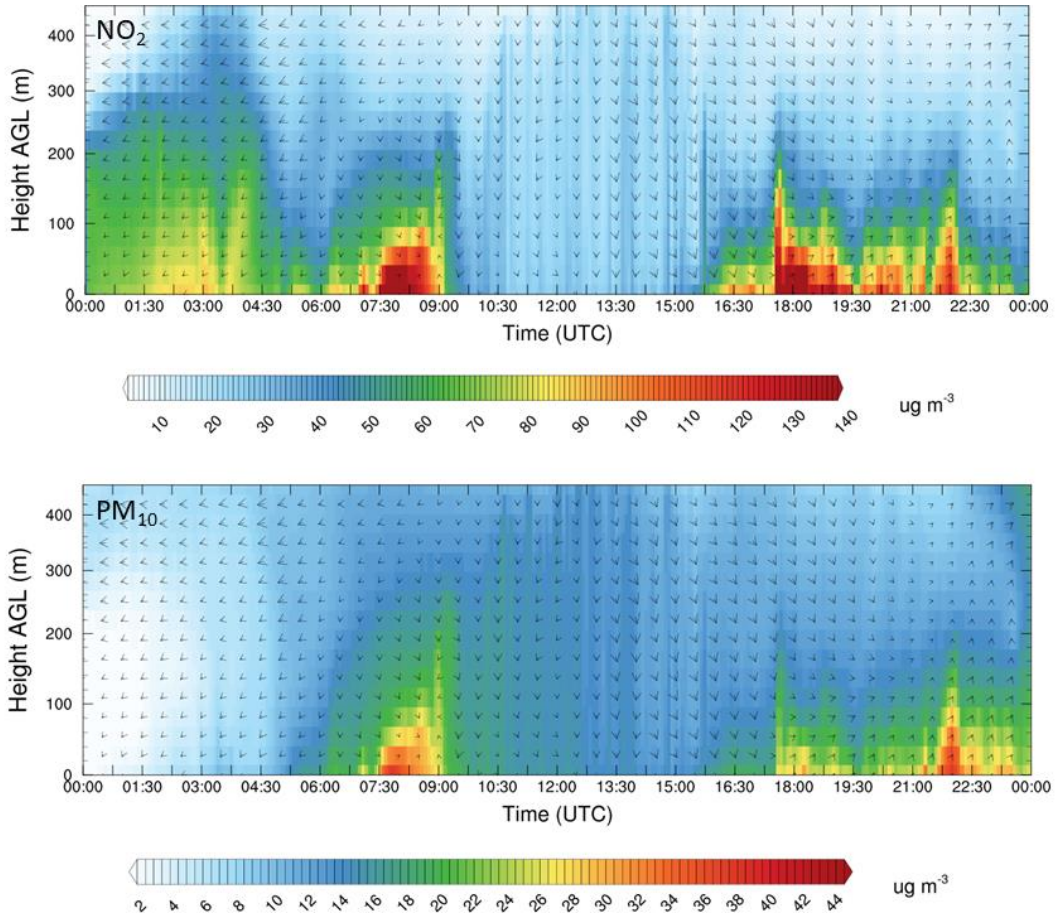

Fig. 16: Time height cross section of NO_2 (top) and PM_{10} (bottom) at Neckartor (NT) up to an altitude of 450 m AGL.

950